Draft version March 1, 2022
Typeset using LaTeX default style in AASTeX62

arXiv:1905.02232v2 [astro-ph.GA] 9 May 2019

The Astrochemical Impact of Cosmic Rays in Protoclusters I: Molecular Cloud Chemistry

Brandt A.L. Gaches,[1] Stella S.R. Offner,[2] and Thomas G. Bisbas[3,4]

[1] *Department of Astronomy, University of Massachusetts - Amherst, Amherst, MA 01003, USA*
[2] *Department of Astronomy, The University of Texas at Austin, Austin, TX 78712, USA*
[3] *I. Physikalisches Institut, Universität zu Köln, Zülpicher Straße 77, Germany*
[4] *Department of Physics, Aristotle University of Thessaloniki, GR-54124 Thessaloniki, Greece*

ABSTRACT

We present astrochemical photo-dissociation region models in which cosmic ray attenuation has been fully coupled to the chemical evolution of the gas. We model the astrochemical impact of cosmic rays, including those accelerated by protostellar accretion shocks, on molecular clouds hosting protoclusters. Our models with embedded protostars reproduce observed ionization rates. We study the imprint of cosmic ray attenuation on ions for models with different surface cosmic ray spectra and different star formation efficiencies. We find that abundances, particularly ions, are sensitive to the treatment of cosmic rays. We show the column densities of ions are under predicted by the "classic" treatment of cosmic rays by an order of magnitude. We also test two common chemistry approximations used to infer ionization rates. We conclude that the approximation based on the H_3^+ abundance under predicts the ionization rate except in regions where the cosmic rays dominate the chemistry. Our models suggest the chemistry in dense gas will be significantly impacted by the increased ionization rates, leading to a reduction in molecules such as NH_3 and causing H_2-rich gas to become [C II] bright.

Keywords: astrochemistry, stars: protostars, (ISM:) cosmic rays, ISM: molecules, ISM: abundances

1. INTRODUCTION

Molecular cloud dynamics and chemistry are sensitive to the ionization fraction. The chemistry of molecular clouds is dominated by ion-neutral reactions (Watson 1976) and thus controlled by the ionization fraction. The gas (kinetic) temperature of a typical molecular cloud with an average H-nucleus number density of $n \approx 10^3\,\mathrm{cm}^{-3}$ is approximately 10 K for cosmic-ray ionization rates $\zeta \lesssim 10^{-16}\,\mathrm{s}^{-1}$ (Bisbas et al. 2015, 2017), thus rendering neutral-neutral reactions inefficient. Ionization in molecular clouds is produced in three difference ways: UV radiation, cosmic rays (CRs), and X-Ray radiation. Ultra-violet radiation, from external O- and B-type stars and internal protostars, does not penetrate very far into the cloud due to absorption by dust. However, cosmic rays, which are relativistic charged particles, travel much further into molecular clouds and dominate the ionization fraction when $A_V \geq 5\,\mathrm{mag}$ (McKee 1989; Strong et al. 2007; Grenier et al. 2015). CR-driven chemistry is initiated by ionized molecular hydrogen, H_2^+ (Dalgarno 2006). The ion-neutral chemistry rapidly follows:

$$\mathrm{CR} + \mathrm{H_2} \rightarrow \mathrm{H_2^+} + \mathrm{e^-} + \mathrm{CR'}$$
$$\mathrm{H_2^+} + \mathrm{H_2} \rightarrow \mathrm{H_3^+} + \mathrm{H},$$

where CR′ is the same particle as CR but with a lower energy. The ejected electron from the first reaction can have an energy greater than the ionization potential of H_2 and thus cause further ionization. Once H_3^+ forms, more complex

bgaches@astro.umass.edu
soffner@astro.as.texas.edu
bisbas@ph1.uni-koeln.de; tbisbas@auth.gr
Corresponding author: Brandt Gaches

chemistry follows, thereby creating a large array of hydrogenated ions:

$$X + H_3^+ \rightarrow [XH]^+ + H_2.$$

Both HCO^+ and N_2H^+, important molecules used to map the dense gas in molecular clouds, form this way with X being CO and N_2, respectively. These species are also used to constrain the cosmic ray ionization rate (CRIR) (i.e., Caselli et al. 1998; Ceccarelli et al. 2014). OH^+ and H_nO^+ are also formed this way through H_3^+ and H^+ (Hollenbach et al. 2012). In addition, at low column densities ($A_V < 1$ mag), which is typical of the boundaries of molecular clouds), the non-thermal motions between ions and neutrals may overcome the energy barrier of the reaction

$$C^+ + H_2 \rightarrow CH^+ + H,$$

leading to an enhancement of the CO column density (Federman et al. 1996; Visser et al. 2009) and a shift of the HI-to-H_2 transition to higher A_V (Bisbas et al. 2019).

The ionization fraction controls the coupling of the magnetic fields to the gas, influencing non-ideal magnetohydrodynamic (MHD) effects such as ambipolar diffusion (McKee & Ostriker 2007). These non-ideal effects can play a signficant role in the evolution in the cores and disks of protostars. On galactic scales, numerical simulations have shown that CRs can help drive large outflows and winds out of the galaxy (e.g., Girichidis et al. 2016). Our study focuses on the impact of CRs on Giant Molecular Cloud scales which is typically not resolved fully in such simulations.

There have been a plethora of studies modeling the impact of CRs on chemistry and thermal balance (i.e., Caselli et al. 1998; Bell et al. 2006; Meijerink et al. 2011; Bayet et al. 2011; Clark et al. 2013; Bisbas et al. 2015). However, in these studies, and the vast majority of astrochemical models, the CRIR is held constant throughout the cloud, despite the recognition that CRs are attenuated and modulated while traveling through molecular gas (Schlickeiser 2002; Padovani et al. 2009; Schlickeiser et al. 2016; Padovani et al. 2018). Galactic-CRs, thought to be accelerated in supernova remnants or active galactic nuclei, are affected by hadronic and Coulombic energy losses and screening mechanisms that reduce the flux with increasing column density (Strong & Moskalenko 2001; Moskalenko et al. 2005; Evoli et al. 2017). The modulation of CRs has not previously been included within astrochemical models of molecular clouds due to the difficulty in calculating the attenuation and subsequent decrease in the CRIR (Wakelam et al. 2013; Cleeves et al. 2014).

Given that CRs are thought to be attenuated, it is expected that the ionization rate should decline within molecular clouds. However, recent observations do not universally show a lower ionization rate. Favre et al. (2017) inferred the CRIR towards 9 protostars and found a CRIR consistent with the rate inferred for galactic CRs. The OMC-2 FIR 4 protocluster, hosting a bright protostar, is observed to have a CRIR 1000 higher than the expected rate from galactic CRs (Ceccarelli et al. 2014; Fontani et al. 2017; Favre et al. 2018). Gaches & Offner (2018b) show that this system can be modelled assuming the central source is accelerating protons and electrons within the accretion shocks on the protostar's surface. In general, accreting, embedded protostars may accelerate enough CRs to cancel the effect of the attenuation of external CRs at high column densities, producing a nearly constant ionization rate throughout the cloud (Padovani et al. 2016; Gaches & Offner 2018b).

Typical accretion shocks and shocks generated by protostellar jets satisfy the physical conditions necessary to accelerate protons and electrons (Padovani et al. 2016; Gaches & Offner 2018b). Accretion shocks in particular are a promising source of CRs since they are strong, with velocities exceeding 100 km/s and temperatures of millions of degrees Kelvin (Hartmann et al. 2016). Gaches & Offner (2018b) calculated the spectrum of accelerated protons in protostellar accretion shocks and the attenuation through the natal core assuming that the CRs free-stream outwards. These models suggest that clusters of a few hundred protostars accelerate enough CRs into the surrounding cloud to exceed the ionization rate from Galactic CRs.

In this study, we explore the effects of protostellar CRs on molecular cloud chemistry by employing the model of Gaches & Offner (2018b). We implement an approximation for CR attenuation into the astrochemistry code 3D-PDR (Bisbas et al. 2012) to account for CR ionization rate gradients. We investigate the signatures of a spatially varying ionization rate. We further explore the impact of protostellar CR sources and their observable signatures.

The layout of the paper is as follows. In §2 we present the CR and protostellar models and describe the implementation of CR attenuation into 3D-PDR. We discuss our results in §3. Finally, in §4 we create observational predictions and compare them to observations.

2. METHODS

2.1. *Protocluster Model*

We generate protoclusters following the method of Gaches & Offner (2018a), where the model cluster is parameterized by the number of stars and gas surface density, N_* and $\Sigma_{\rm cl}$, respectively. These parameters are connected to the star formation efficiency $\varepsilon_g = M_*/M_{\rm gas}$, where $M_{\rm gas}$ is related to $\Sigma_{\rm cl}$ following McKee & Tan (2003) $\Sigma_{\rm cl} = \frac{M_{\rm gas}}{\pi R^2}$, where the cloud radius, R, is determined from the density distribution (See §2.3). We model protoclusters with surface densities in the range $0.1 \leq \Sigma_{\rm cl} \leq 10$ g cm^{-2} and with a number of stars in the range $10^2 \leq N_* \leq 10^4$. In this parameter space, we always consider $\varepsilon_g \leq 25\%$.

We generate $N_{\rm cl} = 20$ protoclusters for each point in the parameter space and adopt the average CR spectrum for the chemistry modelling. We use the Tapered Turbulent Core (TTC) accretion history model (McKee & Tan 2003; Offner & McKee 2011), where the protostellar core is supported by turbulent pressure and accretion is tapered to produce smaller accretion rates as the protostellar mass, m, approaches the final mass, m_f. Gaches & Offner (2018a) showed the TTC model is able to reproduce the bolometric luminosities of observed local protoclusters.

2.2. *Cosmic Ray Model*

We brielfy summarize the CR acceleration and propagation model in Gaches & Offner (2018b) and refer the reader to that paper for more details. We assume CRs are accelerated in the accretion shock near the protostellar surface. Accreting gas is thought to flow along magnetic field lines in collimated flows with the shock at the termination of the flow. We assume the shock velocities are comparable to the free-fall velocity at the stellar surface. Following Hartmann et al. (2016), we assume fully ionized strong shocks with the shock front perpendicular to the magnetic field lines. We adopt a mean molecular weight $\mu_I = 0.6$ and a filling fraction of accretion columns on the surface, $f = 0.1$.

We calculate the CR spectrum under the Diffusive Shock Acceleration (DSA) limit, also known as first-order Fermi acceleration (e.g., reviewed in Drury 1983; Kirk 1994; Melrose 2009). Under DSA, the CR momentum distribution is a power-law, $f(p) \propto p^{-q}$, where q is related to the shock properties. We attenuate the CR spectrum through the protostellar core following Padovani et al. (2009). Padovani et al. (2018) presented updated attenuation models for surface densities up to 3000 g cm^{-2}, but the results remain unchanged for the surface of concern in this work. The core surface density and radius for a turbulence-supported core are (McKee & Tan 2003):

$$\Sigma_{\rm core} = 1.22\Sigma_{\rm cl} = 0.122\,{\rm g\,cm^{-2}} \left(\frac{\Sigma_{\rm cl}}{0.1\,{\rm g\,cm^{-2}}}\right) \tag{1a}$$

$$\begin{aligned} N({\rm H_2})_{\rm core} &= \frac{\Sigma_{\rm core}}{\mu_M m_H} \\ &= 3\times10^{22}\,{\rm cm^{-2}} \left(\frac{\Sigma_{\rm core}}{0.122\,{\rm g\,cm^{-2}}}\right)\left(\frac{2.4}{\mu}\right) \end{aligned} \tag{1b}$$

$$\begin{aligned} R_{\rm core} &= 0.057\Sigma_{\rm cl}^{-\frac{1}{2}} \left(\frac{m_f}{30\ M_\odot}\right)^{\frac{1}{2}}\ {\rm pc} \\ &= 0.104\,{\rm pc}\left(\frac{\Sigma_{\rm cl}}{0.1\,{\rm g\,cm^{-2}}}\right)^{-\frac{1}{2}}\left(\frac{m_f}{10\,{\rm M_\odot}}\right)^{\frac{1}{2}}, \end{aligned} \tag{1c}$$

where $\mu_M = 2.4$ is the mean molecular weight for a molecular gas. We calculate the total protocluster CRIR by summing over the N_* attenuated CR spectra.

2.3. *Density Structure*

We assume the molecular cloud density is described by an inverse power law

$$n(r) = n_0\left(\frac{R}{r}\right)^2, \tag{2}$$

where R is the cloud radius and n_0 is the number density with an inner radius of 0.1 pc. The r^{-2} dependence matches the solution for isothermal collapse (Shu 1977). We take $n_0 = 100$ cm^{-3}, corresponding to a gas regime in which the cloud is expected to be mostly molecular under typical conditions. The radius is set by constraining the total surface density by $\Sigma_{\rm cl}$ as defined:

$$\int_{R_c}^{R} n(r)dr = \frac{\Sigma_{\rm cl}}{\mu_M m_H}, \tag{3}$$

Table 1. Atomic Abundances

Species	Abundance Relative to H
H	1.0
He	0.1
C	1.41×10^{-4}
N	7.59×10^{-5}
O	3.16×10^{-4}
S	1.17×10^{-5}
Si	1.51×10^{-5}
Mg	1.45×10^{-5}
Fe	1.62×10^{-5}

NOTE—Atomic abundances adopted from Sembach et al. (2000).

where R_c is the inner radius delineating the transition between the molecular cloud and protostellar core. The turbulent-linewidth, σ, of a cloud with density profile $n(r) \propto r^{-2}$ and a virial α parameter is (Bertoldi & McKee 1992):

$$\sigma = \left(\frac{GM^2\alpha}{3\mu_M m_H \bar{n} V R}\right)^{\frac{1}{2}}, \tag{4}$$

where $\bar{n}$ is the volume-averaged density from $n(r)$, G is the gravitational constant, and $V = \frac{4}{3}\pi R^3$ is the volume of the molecular cloud. We take $\alpha = 2$ for our fiducial model (Heyer & Dame 2015).

2.4. *Chemistry with Cosmic Ray Attenuation*

We use a modified version of the 3D-PDR astrochemistry code[1] introduced in Bisbas et al. (2012). 3D-PDR solves the chemical abundance and thermal balance in one-, two- and three-dimensions for arbitrary gas distributions. The code can be applied to arbitrary three dimensional gas distributions, such as post-processing simulations (Offner et al. 2013, 2014; Bisbas et al. 2018). Here, we use the code in one dimension to model a large parameter space. We adopt the McElroy et al. (2013) UMIST12 chemical network containing 215 species and approximately 3,000 reactions. We assume the gas is initially composed of molecular H_2 with the rest being atomic with abundances from Sembach et al. (2000) shown in Table 1. Cooling is included from line emission, which is mainly due to carbon monoxide at low temperatures and forbidden lines of [OI],[CI] and [CII] at higher temperatures. Heating is due to dissipation of turbulence, photoelectric heating of dust from far-ultraviolet emission, H_2 fluorescence and CR heating of gas. We use a temperature floor of 10 K. Previously, 3D-PDR included CRs via a single global CRIR parameter. See Bisbas et al. (2012) for more technical details.

We modify 3D-PDR to account for CR attenuation through the cloud. Currently, our implementation is restricted to one-dimensional models where we assume spherical symmetry. 3D-PDR calculates the CRIR from $N_{\rm SRC}$ CR sources. The user provides a CR spectrum for any number of sources and whether it is external (incident at the surface) or internal (originating at the cloud center). In 1D, the fluxes are defined on either surface of the domain. The flux due to external sources is attenuated while the point sources are assumed to radiate isotropically; both are attenuated and spatially diluted. The spectra are attenuated after every update of the molecular abundances to keep the amount of H_2 for interaction losses self-consistent. 3D-PDR stores the initial CR flux in $N_{\rm ene}$ bins and self-consistently calculates ζ from all sources across the domain. Point sources require a user-set radial scaling factor, r_s, and a transport parameter, a. For our model results, we set $r_s = R_C$ to represent the core radius. Point source CR spectra, $j(E, r)$, are attenuated by the H_2 column density (Padovani et al. 2009) and diluted by the radial distance following

$$j(r) \propto \left(\frac{r_s}{r + r_s}\right)^a, \tag{5}$$

[1] The code can be downloaded from https://uclchem.github.io, including the new modifications presented in this paper.

Table 2. Model Parameters

Parameter	Definition	Fiducial Value
$\mu_{\rm I}$	Reduced gas mass	0.6 (ionized)
$\mu_{\rm M}$	Reduced gas mass	2.4 (neutral molecular)
n_0	Density at edge of cloud	10^2 cm^{-3}
$N_{\rm src}$	Number of CR Sources	2
$N_{\rm bins}$	Number of CR spectrum bins	40
a	CR transport parameter	1
r_s	Scaling radius for CR flux	0.1 pc
α	Cloud virial parameter	2

to approximate the effects of transport. Solving the transport equations for Galactic transport problems has been done with specialized codes, such as GALPROP (Moskalenko & Strong 1998) and DRAGON2 (Evoli et al. 2017). Fully solving the steady-state transport equations are beyond the scope of this work but will be investigated in the future.

In our study, we include two CR flux sources. First, we include the internal protostellar clusters discussed above. We set the radial scaling $r_s = R_C = 0.1$ pc, which is approximately the size of a protostellar core. Second, we include an external isotropic CR flux to model interstellar CRs. We follow Ivlev et al. (2015) and parameterize the external flux as

$$j_{\rm ext} = C\frac{E^\alpha}{(E+E_0)^\beta} \quad \text{(particles eV}^{-1}\text{ cm}^{-2}\text{ s}^{-1}\text{ sr}^{-1}\text{)}. \tag{6}$$

We use their "low" model ($\mathcal{L}$), with $C = 2.4\times10^{15}$, $E_0 = 650$ MeV, $\alpha = 0.1$ and $\beta = 2.8$ and their "high" model ($\mathcal{H}$), with $C = 2.4\times10^{15}$, $E_0 = 650$ MeV, $\alpha = -0.8$ and $\beta = 1.9$. The $\mathcal{L}$ model is a direct extrapolation of the Voyager-1 data (Stone et al. 2013), while the $\mathcal{H}$ is a maximal model to correct for any possible effects of the solar magnetic field. The CRIR is calculated by integrating the spectrum multiplied by the H_2 cross section:

$$\zeta_p = 2\pi\int j(E)\sigma_i(E)dE, \tag{7}$$

where the factor of 2π accounts for irradiating the 1-D surface on one side and $\sigma_i(E)$ is the H_2 ionization cross section with relativistic corrections (Krause et al. 2015). The code allows for an arbitrary number of energy bins, $N_{\rm bins}$, for input CR spectrum. We compared the CRIR for bin sizes ranging from $N_{\rm bin} = 4$ to 1000 and found that $N_{\rm bins} > 40$ only produces changes in the CRIR at the 1% level. We do not fully solve for primary or secondary electrons. Therefore, we multiply the proton CRIR by $\frac{5}{3}$ to account for the electron population (Dalgarno & Griffing 1958; Takayanagi 1973).

Our fiducial parameters for the study are shown in Table 2. Table 3 shows the full suite of models we adopt. The model names describe the included physics: L/H denotes using the $\mathcal{L}/\mathcal{H}$ (Low/High) external spectrum, NI denotes no internal sources, DI denotes internal sources with $a = 1$ (diffusive transport), RI denotes internal sources with $a = 2$ (rectilinear transport) and NA denotes no internal sources or CR attenuation. We study the impact of these parameters in Section 3.

3. RESULTS

3.1. *Cosmic Ray Spectrum*

Our modified 3D-PDR code requires as an input the flux of CR protons for any number of sources. As a result, the CR proton flux and CRIR throughout the spatial domain become outputs rather than inputs. Figure 1 shows an example CR spectrum for a molecular cloud with $\Sigma_{\rm cl} = 0.75$ g cm^{-2} and $N_* = 750$ using the LDI model. The CR proton flux increases inside the cloud because of the embedded sources. The double peaked shape of the spectrum is due to peaks in the loss function from ionization and Coulomb losses. The inset shows the CRIR as a function of the position within the cloud. In this model, the ionization rate climbs nearly two orders of magnitude throughout the cloud with increasing proximity to the protostellar cluster.

Table 3. Models examined. L/H denotes Low/High external spectrum, NI denotes no internal sources, DI denotes internal sources with $a = 1$ (diffusive transport), RI denotes internal sources with $a = 2$ (rectilinear transport) and NA denotes no internal sources or CR attenuation.

Name	Source Transport	Internal	External Field	Attenuation
LDI	r^{-1}	✓	$\mathcal{L}$	✓
LRI	r^{-2}	✓	$\mathcal{L}$	✓
LNI	...	...	$\mathcal{L}$	✓
LNA	...	...	$\mathcal{L}$	...
HNI	...	...	$\mathcal{H}$	✓
HDI	r^{-1}	✓	$\mathcal{H}$	✓

3.2. *Cosmic Ray Ionization Rate Models*

A number of prescriptions have been used to calculate the CRIR from observed column densities of various tracer species (Caselli et al. 1998; Indriolo & McCall 2012). The inclusion of CR attenuation allows us to directly test the accuracy of these approximations. Our astrochemical models provide the abundances throughout the cloud and the local CRIR in-situ. We test two different prescriptions that are typically used for diffuse and dense gas, respectively, from Indriolo & McCall (2012). The first, and simplest, denoted as "Simple Electron Balance" (SEB), estimates the CRIR using only the abundance of H_3^+ and e^-:

$$\zeta = k_e n(\mathrm{e}^-) \frac{n(\mathrm{H}_2)}{n(\mathrm{H}_3^+)}, \tag{8}$$

where k_e is the H_3^+ electron-recombination rate and $n(\mathrm{e}^-)$, $n(\mathrm{H}_2)$ and $n(\mathrm{H}_3^+)$ are the densities of electrons, molecular hydrogen and H_3^+, respectively. The second approximation includes the destruction of H_3^+ with CO and O, which we denote the "Reduced Analytic" (RA) model:

$$\zeta = \frac{x(\mathrm{H}_3^+)}{x(\mathrm{H}_2)} n_H \left[k_e x(\mathrm{e}^-) + k_{\mathrm{CO}} x(\mathrm{CO}) + k_O x(\mathrm{O})\right] \times \left[1 + \frac{2k_3 x(\mathrm{e}^-)}{k_2 f(\mathrm{H}_2)} + \frac{2k_4}{k_2}\left(\frac{1}{f(\mathrm{H}_2)} - 1\right)\right], \tag{9}$$

where k_i are the reaction rate coefficients for the reactions in Table from Indriolo & McCall (2012) (repeated in Table 3.2 below), x_i is the abundance of species i with respect to total Hydrogen nuclei and $f(\mathrm{H}_2) = 2n(\mathrm{H}_2)/n_H$ is the molecular hydrogen fraction.

Figure 2 shows the calculated CRIR using the full model and the approximations in Equations 8 and 9 as a function of the H_3^+ abundance. We show the cases of four different CR models: LNA, LNI, LDI and HDI. The first model, LNA, is of particular importance since it represents the simplest one-dimensional PDR model. Observations typically assume 0D distribution, such that the ratio of column densities is equal to the ratio of the abundances. This makes a tacit assumption that the ionization rate is the same throughout the domain. We find that both approximations produce a large range of CRIRs – even when the input CRIR is fixed due to other effects impacting the chemistry, notably the influence of the external FUV radiation. *The SEB and RA approximation models systematically underestimate the CRIR and produce an artificial spread in the inferred CRIR.* When internal sources are included, we find that both approximations infer the CRIR reasonably well. When there are no internal sources, both approximations underestimate the CRIR by up to an order of magnitude and in general do not represent any real spread in the CRIR accurately.

3.3. *Impact of Cosmic Ray Sources on Cloud Chemistry*

We examine in detail two different CR models: the traditional LNA and the LDI model. Figure 3 shows the column densities of different species and density averaged temperature and CRIR for the LNA model as a function of Σ_{cl} and N_*. The total column density of each species increases with the gas surface density, Σ_{cl}, and hence the total gas mass. Furthermore, we find across the whole parameter space that $\mathrm{N(CO)} > \mathrm{N(C)} > \mathrm{N(C^+)}$. This qualitative behavior is to

Table 4. Reactions for Reduced Analytic H_3^+ Chemistry

Reaction	Rate Coefficient (cm^3 s^{-1})	Reference
$H_2^+ + H_2 \rightarrow H_3^+ + H$	$k_2 = 2.09 \times 10^{-9}$	Theard & Huntress (1974)
$H_2^+ + e^- \rightarrow H + H$	$k_3 = 1.6 \times 10^{-8}(T/300)^{-0.43}$	Mitchell (1990)
$H_2^+ + H \rightarrow H_2 + H^+$	$k_4 = 6.4 \times 10^{-10}$	Karpas et al. (1979)
$H_3^+ + e^- \rightarrow$ products	$k_5 = k_e = -1.3 \times 10^{-8} + 1.27 \times 10^{-6} T_e^{-0.48}$	McCall et al. (2004)
$H_3^+ + CO \rightarrow H_2 + HCO^+$	$k_6 = 1.36 \times 10^{-9}(T/300)^{-0.142} \exp 3.41/T$	Klippenstein et al. (2010)
$H_3^+ + CO \rightarrow H_2 + HCO^+$	$k_7 = 8.49 \times 10^{-10}(T/300)^{0.0661} \exp -5.21/T$	Klippenstein et al. (2010)
$H_3^+ + O \rightarrow H_2 + OH^+$	$k_8 = k_O = 1.14^{-9}(T/300)^{-0.156} \exp -1.41/T$	Klippenstein et al. (2010)

NOTE—Equations 8 and 9 reactino rates where $k_{CO} = k_6 + k_7$ in Equation 9. We omit the Nitrogen reaction from Indriolo & McCall (2012) Table 3 since it is not in use by either approximation.

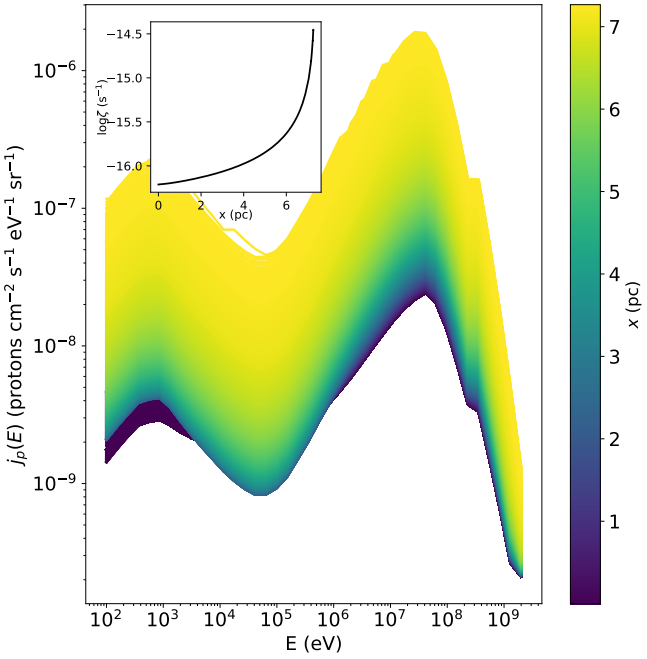


Figure 1. Proton cosmic ray spectrum with line color indicating position within the cloud for $\Sigma_{cl} = 0.75$ g cm^{-2} and $N_* = 750$ using the LDI CR model. Inset: Cosmic ray ionization rate versus position, x, into the cloud, where $x = 0$ is the cloud surface.

be expected with no internal sources. Figure 4 shows the abundance profiles for the LNA model as a function of A_V into the cloud, Σ_{cl} and N_*. Since there are no embedded sources in this model, there is no difference between models of different N_*. The abundance profiles for C^+, C and CO exhibit the expected "layered" behavior (Draine 2011): C^+ is confined to the surface, C exists in a thin, warm layer and CO asymptotically approaches an abundance of $[CO/H_2] \approx 10^{-4}$. Similarly the abundance of NH_3 steadily increases into the cloud.

The abundance ratio $[HCO^+/N_2H^+]$ is sometimes used to infer the CRIR under the assumption the two molecules are co-spatial (i.e., Ceccarelli et al. 2014). We find that, while they share some local maxima, they are not completely co-spatial in agreement with the turbulent cloud study of Gaches et al. (2015).Moreover, observations show that while they are not entirely co-spatial, there is overlap in the emission regions (i.e., Jørgensen 2004; Ceccarelli et al. 2014; Storm et al. 2016; Favre et al. 2017; Pety et al. 2017; Pound & Yusef-Zadeh 2018). In particular, we show HCO^+ can

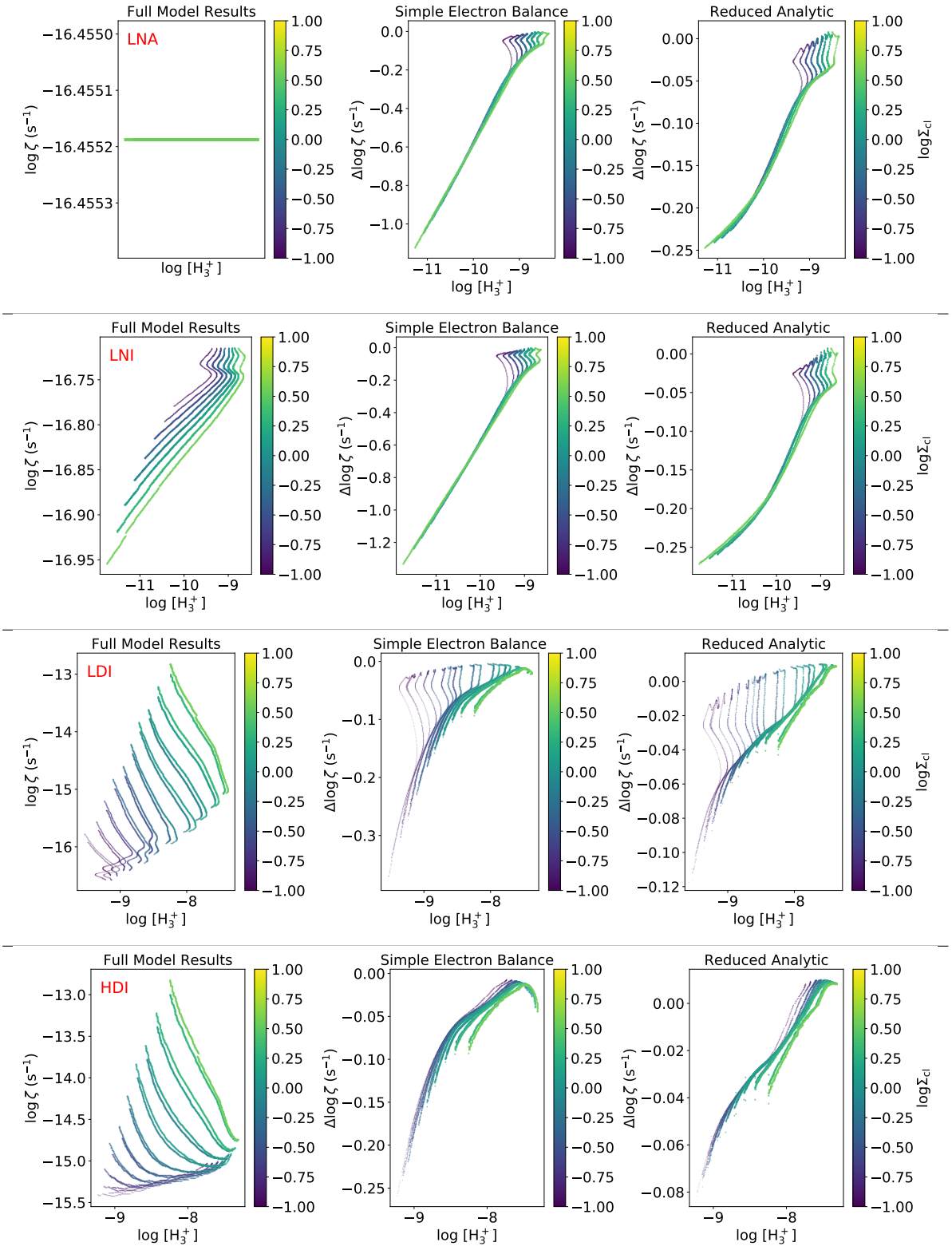


Figure 2. Left: Cosmic ray ionization rate as a function of H_3^+ abundance using the full astrochemical model results. Middle: Relative logarithmic error in ζ, $\Delta \log \zeta$, calculated using electron-balance approximation (Equation 8) and full astrochemical model. Right: Same as middle row but using the reduced analytic approximation (Equation 9). Color: Gas surface density, $\Sigma_{\rm cl}$ in g cm^{-2}. Models in descending order from the top are: LNA, LNI, LDI, HDI.

exist at much lower A_V than N_2H^+. Due to similar critical densities however, the two molecules thermalize at nearly the same densities.

Figure 5 shows the column densities across the parameter space for the LDI model. Here we find a very different behavior compared to the LNA model shown in Figure 3, where the differences are especially pronounced for the more diffuse gas tracers. The column densities are no longer strictly functions of $\Sigma_{\rm cl}$ but depend on N_*. For large, massive star-forming regions (upper right corner in each panel), the gas becomes CO deficient and C rich while the bulk of gas remains molecular. Similarly, there is a slight increase in the column density of HCO^+ and N_2H^+ due to the increase in ionization. The qualitative trends exhibited by C^+, C, and marginally by HCO^+ and N_2H^+, follow that of the density-averaged CRIR, $\langle\zeta_\rho\rangle$.

The effect of an embedded protocluster is also visible in the abundance profiles. Figure 6 shows the abundance profiles for the LDI model. We find that CO only approaches abundances of 10^{-4} for clusters with little embedded star formation.For smaller mass clouds (i.e., smaller $\Sigma_{\rm cl}$), the C^+, C and CO abundance remains fairly unchanged compared to the LNA model. In the most massive clouds, the amount of CO at $A_V \leq 1$ is enhanced by an order of magnitude and reduced by an order of magnitude at $A_V \geq 5$. We further see a reduction in N_2H^+ at mid-A_V with an enhancement of HCO^+. Likewise the gas temperature exceeds $T > 30$ K for most of the clouds with $\Sigma_{\rm cl} > 0.25$ g cm^{-2}. As $A_V \rightarrow 10^3$, the differences between the molecular ion abundances is much less due to the greatly increased density compared to the surface of the cloud. The abundance of H_2 in the dense gas is unaffected by the increased CRIR.

We now statistically quantify the impact of different CR models on the six different molecules: C^+, C, CO, N_2H^+, HCO^+ and H_3^+. We investigate the H_3^+ column density because it is the simplest molecule that can be used to constrain the CRIR (Dalgarno 2006). We calculate the column density logarithmic difference:

$$\Delta_s = \log \frac{N_{s,i}}{N_{s,\rm LNA}}, \tag{10}$$

with s representing the different species, and i the different CR models exluding the LNA model. Figure 7 shows violin plots representing the probability distribution of Δ_s using all clouds in the $(\Sigma_{\rm cl} - N_*)$ space. In all cases, CO is never enhanced but rather depleted. This is because the maximum abundance [CO] $= 10^{-4}$ is set by the C/O ratio. Our models generally increase the local CRIR, thereby dissociating the CO and reducing its abundance. We find very little difference between the LNI and LNA for all molecules except for N_2H^+ and HCO^+, which exhibit a 25% linear dispersion. This is caused by the impact of higher ionization rates towards the surface of the clouds. The HNI model,which has the highest overall CRIR at the surface, shows a clear offset for the atomic and ionic species and a slight deficit for CO. In models LRI, LDI and HDI there is a significant dispersion in the column density difference, Δ_s, in all species. Figure 7 demonstrates that considerable care must be taken when modeling observed column densities of atomic or ionic species: the possible error, Δ_s, in the modeled column densities may be off by an order of magnitude depending on the transport of the cosmic rays and the amount of ongoing embedded star formation. The CRIR is not the only factor that leads to the creation of molecular ions, as typically assumed in observational studies. The abundances are influenced by the FUV flux, which is also enhanced by a central protocluster (Gaches & Offner 2018a).

3.4. *Abundance Ratio Diagnostics for the Cosmic Ray Ionization Rate*

Line and abundance ratios of various tracers are often used to constrain the CRIR in dense gas. The species are typically assumed to be co-spatial (although as demonstrated in Section 3.3 that is not typically the case). We examine two different ratio diagnostics: global diagnostics using column densities and local diagnostics using the local abundance ratios and CRIRs.

Figure 8 shows three different column density ratios for the LNA, LNI and HNI models: [HCO^+/N_2H^+], [CO/C^+] and [C/C^+]. We find that the column density ratios in these cases increase monotonically with $\Sigma_{\rm cl}$. The ratio of [HCO^+/N_2H^+] is nearly constant, changing by less than a factor of two across two dex of $\Sigma_{\rm cl}$. The HNI case shows a slightly different behavior with a slight local minimum in [HCO^+/N_2H^+] at $\Sigma_{\rm cl} = 6$ g cm^{-2}. The trends in these models are not due to changes in the CRIR but rather in the total amount of gas column. The [CO/C^+] ratio shows a buildup of CO compared to C^+. This is to be expected in an externally irradiated model: C^+ remains consistently on the surface, while the amount of CO continues to build with $\Sigma_{\rm cl}$ with a proportional increase in the amount of dense gas. Similarly, the [C/C^+] remains fairly constant since these species exist only in limited areas of A_V.

Figure 9 shows the same column density ratios for three models including the embedded protoclusters: LRI, LDI and HDI. Here the trends are significantly more complicated. The [HCO^+/N_2H^+] ratio still only varies by a factor

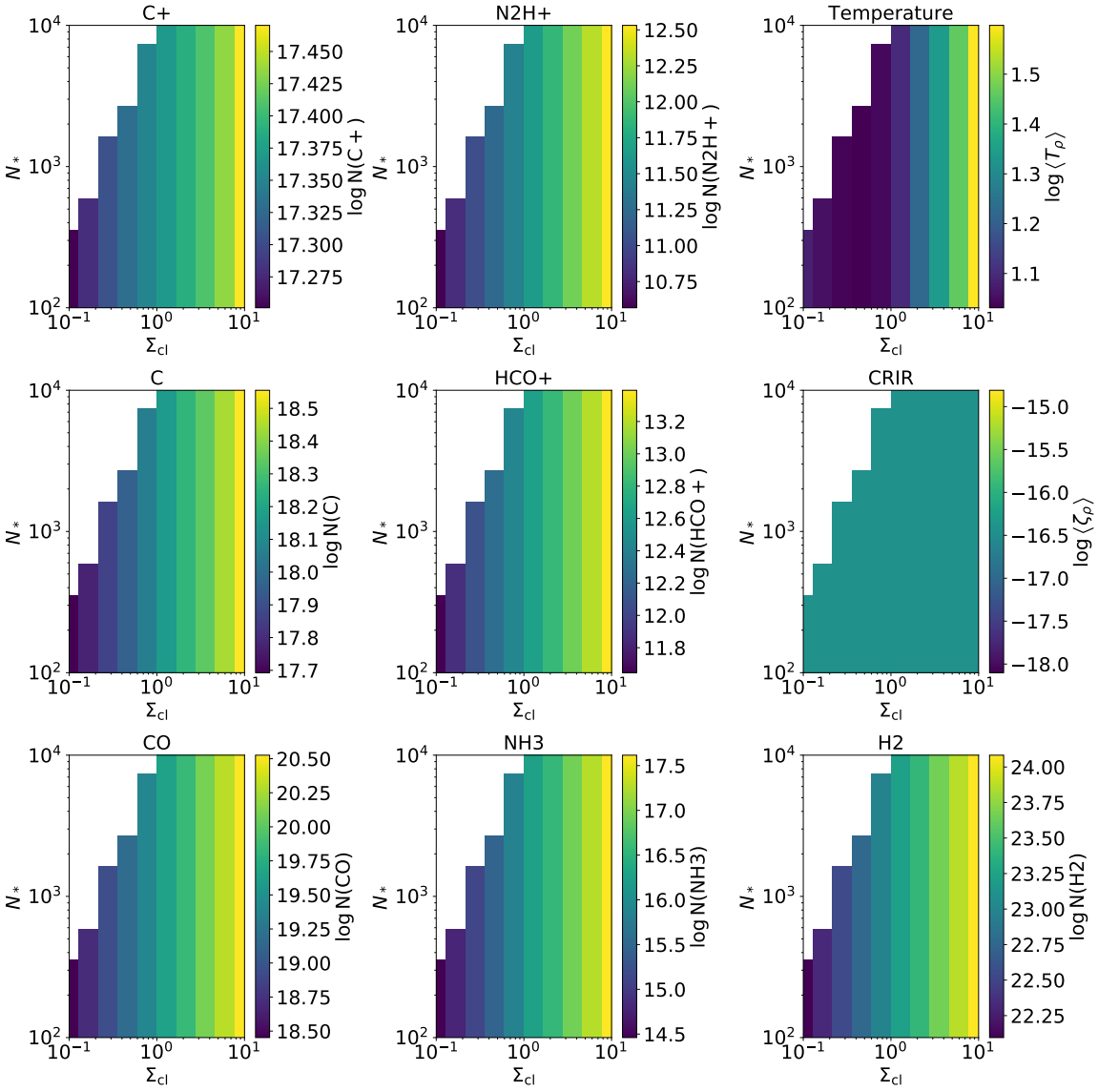


Figure 3. Column density of different molecular species as a function of the number of stars in the protocluster, N_* and the mass surface density, $\Sigma_{\rm cl}$ for the LNA model. The last 3 panels on the far right show the density averaged temperature, CRIR and the total gas column density.

of two throughout the parameter space, but it exhibits more complex behavior. The ratio decreases with $\Sigma_{\rm cl}$ and rises with N_* up to some maximum, with an additional increase in $[HCO^+/N_2H^+]$ for $N_* \approx 10^4$ for the LDI and HDI model. To understand this, we can look at the abundance profiles of the LDI model in detail in Figure 6. The abundance of HCO^+ increases with both with $\Sigma_{\rm cl}$ and N_* with the abundance profile flattening as a function of A_V for $\Sigma_{\rm cl} > 1$ g cm^{-2}. For N_2H^+ the trends are separated by an A_V threshold at $A_V = 1$. At $A_V < 1$, the abundance of N_2H^+ increases like HCO^+, with $\Sigma_{\rm cl}$ and N_*. For $1 < A_V < 100$, the abundance of N_2H^+ is sensitive primarily to N_*. In high ionization environments, CO will be destroyed in the creation of HCO^+ due to interactions with H_3^+. These environments will also produce N_2H^+ which destroys CO to create HCO^+. This is likely the main driving cause in the abundance profiles: there is a reduction of CO and N_2H^+ in the dense more ionized gas, and an systematic increase in HCO^+. The $[CO/C^+]$ ratio increases monotonically across two orders of magnitude towards high $\Sigma_{\rm cl}$ and low N_*: cold gas is less ionized (lower right corner), so the amount of CO increases with respect to C^+. $[C/C^+]$ shows a different trend compared to $[CO/C^+]$. High ionization rates, in both the LDI and HDI models, have an increased $[C/C^+]$ in lower mass clouds hosting smaller clusters and a decreased $[C/C^+]$ at high $\Sigma_{\rm cl}$ compared to the LRI model.

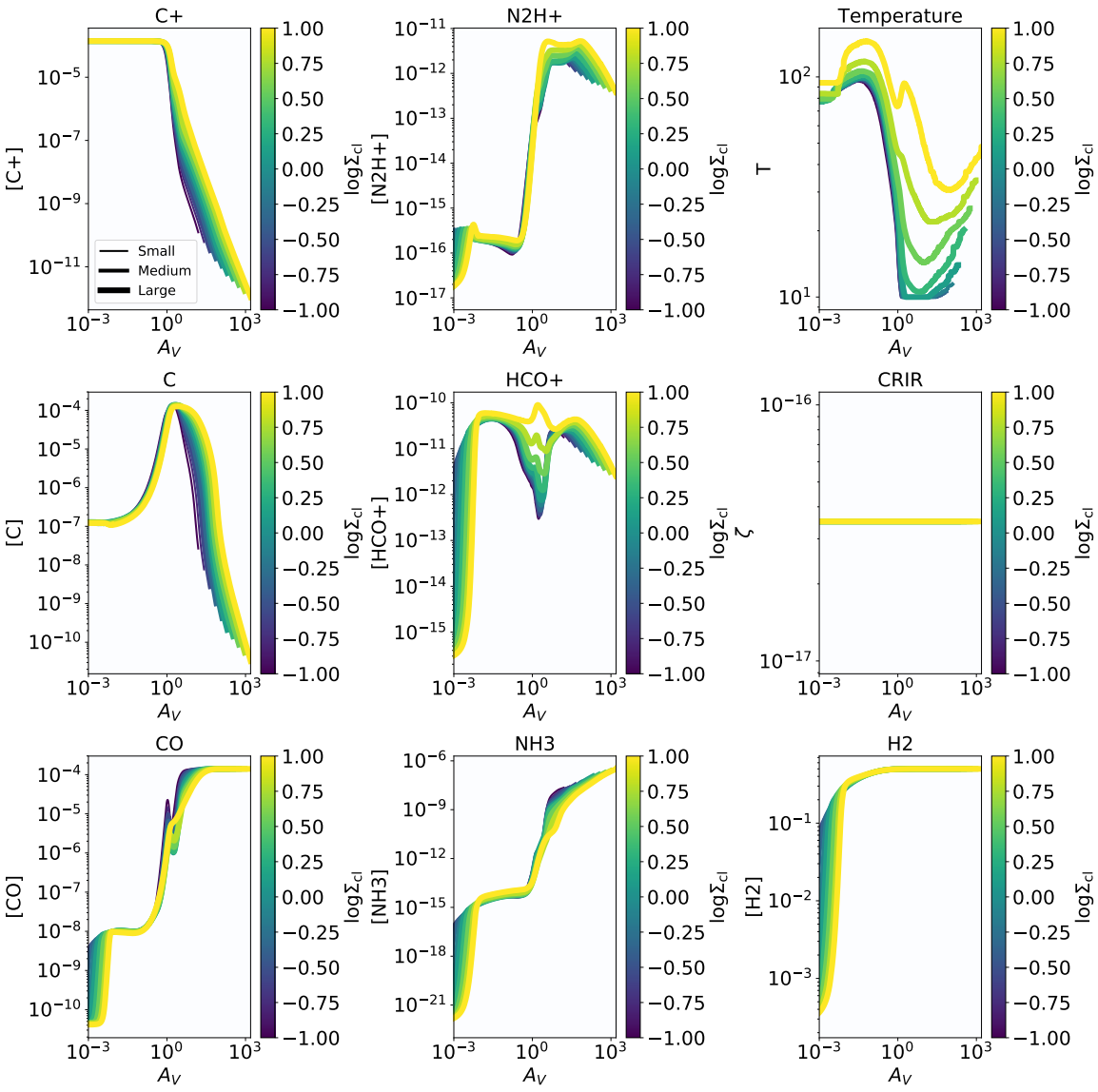


Figure 4. The abundances, [X], for various molecular species, as a function of the visual extinction into the cloud, A_V, for the LNA model. The top two panels on the right column show the temperature and CRIR as a function of the A_V. The colorbar indicates the gas surface density, $\Sigma_{\rm cl}$. The line width indicates the number of protostars in the cluster with "Small" = 10^2, "Medium" = 10^3 and "Large" = 10^4 protostars.

The $[C/C^+]$ ratio is nearly flat across the $\Sigma_{\rm cl} - N_*$ parameter space in the HDI model. Clouds with fewer CRs and more gas shielding to the incident the FUV radiation have more C compared to C^+.

Observational measurements of ζ in dense gas typically use astrochemical modeling and local abundance ratios (See §4.2). Figure 10 plots the CRIR for models with $5\% \leq \varepsilon \leq 25\%$ as a function of different abundance ratios. A good CRIR indicator should exhibit a monotonic trend in response to changes in the CR flux. The LNI model does not exhibit much change in the CRIR, so the local trends depend on density and radiative effects. In the HNI model, only the $[HCO^+/CO]$ ratio exhibits a monotonic trend.

The models with sources show completely different abundance ratios because the dense gas is warmer and the ionization rates are higher. In all of these cases, the ratios are monotonic for $\Sigma_{\rm cl} \gtrsim 1$ g cm^{-2}. For $\Sigma_{\rm cl} \lesssim 1$ g cm^{-2} each exhibits a similar trend as in the NI model subsets. This demonstrates that these diagnostics only constrain regimes where the CRIR influences the chemistry more than radiative or other heating processes.

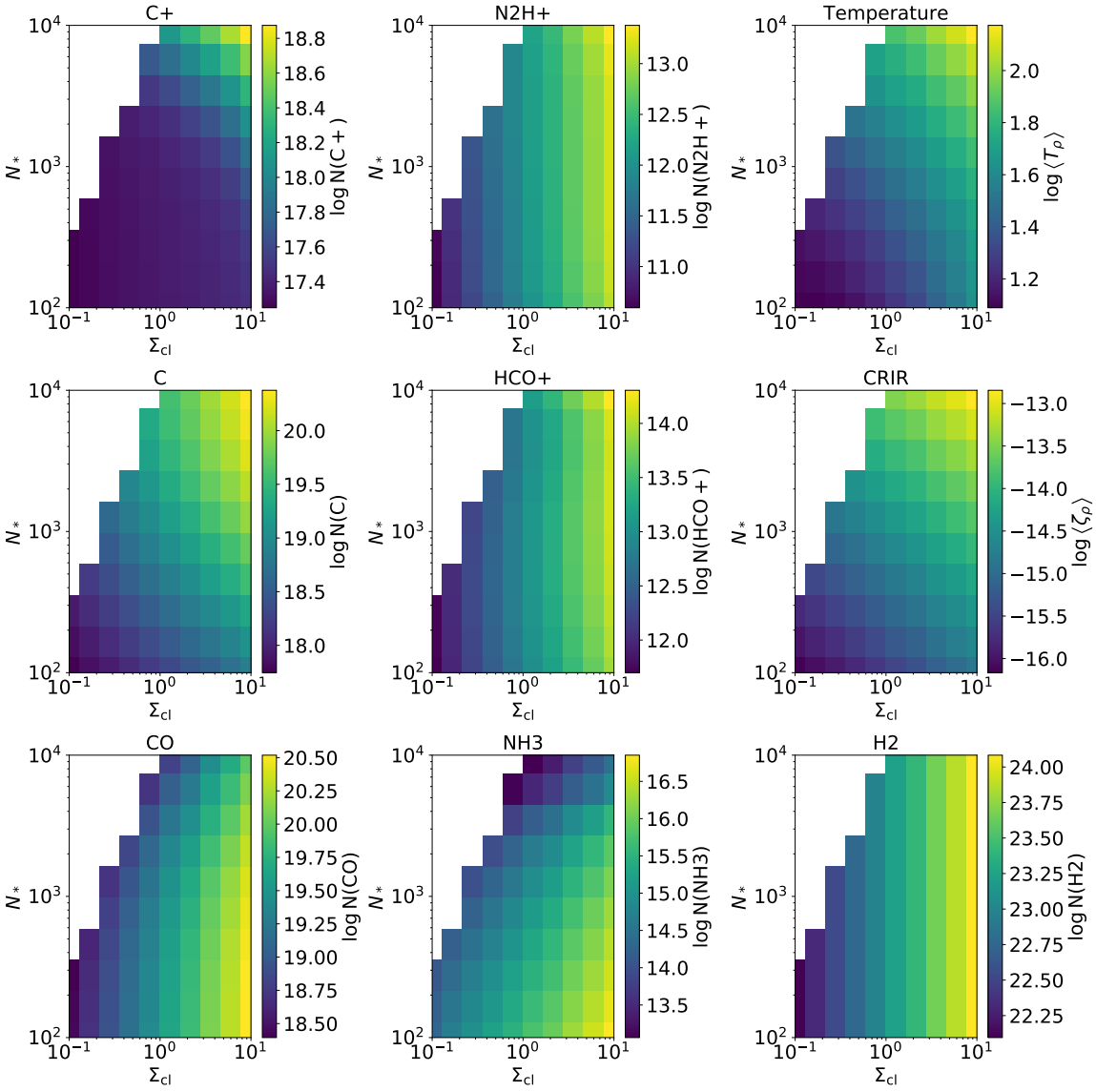


Figure 5. Same as Figure 3 but for model LDI.

4. DISCUSSION

4.1. *Model Assumptions and Caveats*

Our models require a variety of assumptions. First and most importantly, the models are one-dimensional and we assume protostars are clustered in the center. In reality, protostars are distributed throughout molecular clouds. Furthermore, the density distribution of molecular clouds is set by turbulence and is not a purely radial distribution. However, our results will hold qualitatively for the molecular gas around young, dense embedded clusters in molecular clouds, such as the central cluster in ρ Oph. Second, our chemical network does not include any gas-grain chemistry or freeze-out (see McElroy et al. 2013). Therefore, we over-predict the CO abundance in regions where $n > 10^4$ cm^{-3} and $T \lessapprox 30$ K (van Dishoeck 2014). Comparing this criteria to the temperature profiles in Figure 6 shows the models with $\Sigma_{cl} < 0.5$ g cm^{-2} and where $1 \leq A_V \leq 10$ are below the freeze-out temperature. When embedded sources are included, the densest gas heats to temperatures > 50 K. These temperatures lead to desorption from the grains, producing gas-phase CO: any CO-ice that formed before star formation occured would be evaporated back into the gas phase (Jørgensen et al. 2013, 2015).

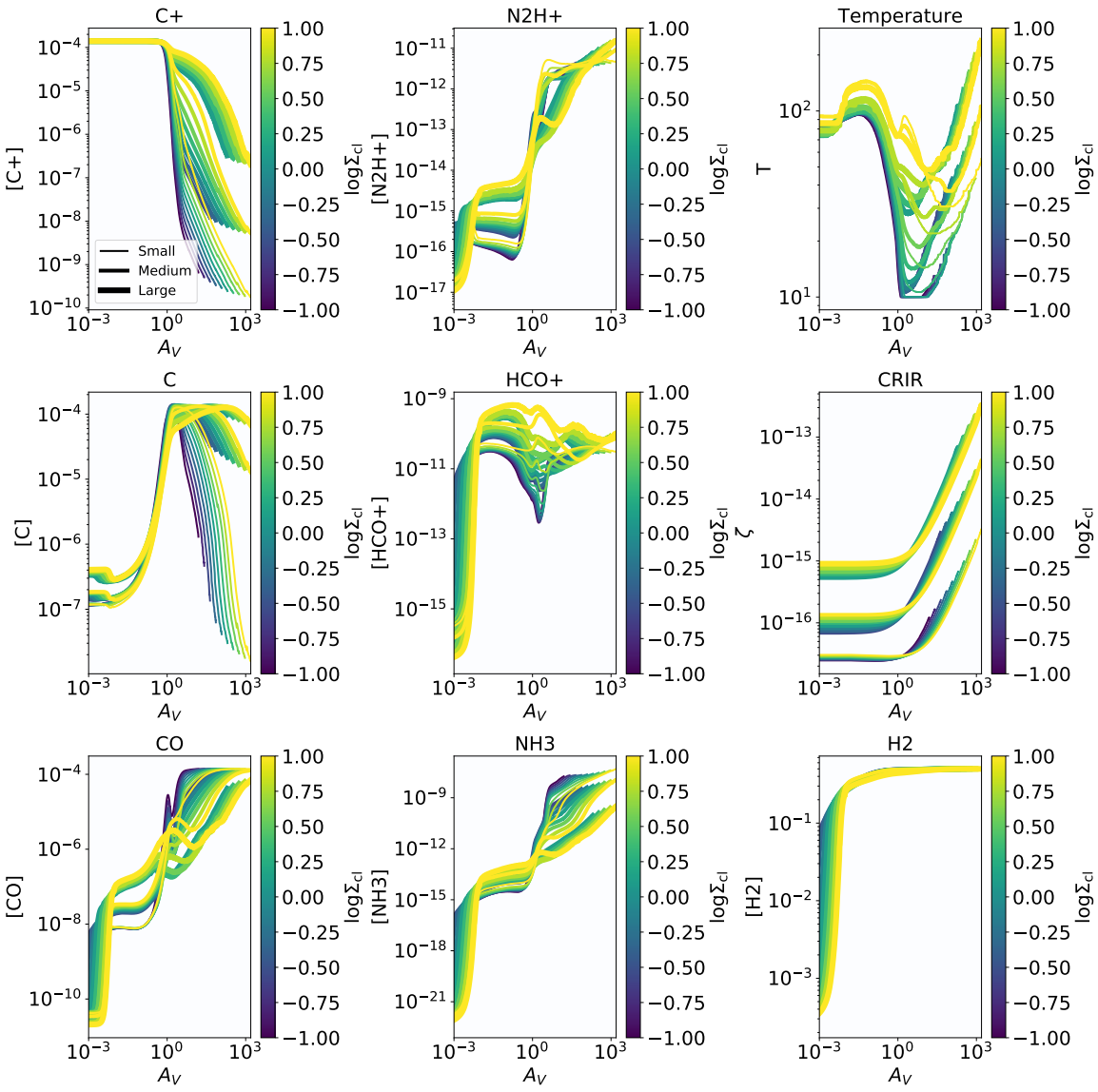


Figure 6. Same as Figure 4 but for model LDI.

We do not fully solve the cosmic ray transport equations or the acceleration dynamics of protons in protostellar accretion shocks. We use analytic approximations to describe the acceleration of CRs at the protostellar shock and the transport out of both the parent core and cloud. Gaches & Offner (2018b) explore the changes in the CRIR for different transport regimes, shock efficiencies and magnetic fields. Differences in the protostellar magnetic field changes the maximum energy of the accelerated CRs but has little effect on the CRIR. However, the CRIR scales nearly linearly with the shock efficiency. Our results assume CR transport in the rectilinear regime through the core. More diffusive transport would produce higher temperatures at the surface of the core than observed. The details of the transport depend both on the magnetic field morphology and on the coupling between the particles and the field. In molecular clouds, turbulence is much stronger than in the cores allowing CRs to diffuse across magnetic field lines rather than streaming along them (Schlickeiser 2002). Conversely, if the particles are well-coupled their trajectories would follow the field lines, potentially producing asymmetries in the CR flux. The directionality imposed by the protostellar outflow could cause CR beaming in the outflow direction or simply advect the particles along with the outflow gas (Rodgers-Lee et al. 2017). We assume CRs transport from their parent cores through the clouds by parameterizing the radial scaling by either diffusive ($1/r$) or free-streaming ($1/r^2$). We do not fully solve the transport equations, which has yet to be done for CRs propagating out of molecular clouds from internal sources.

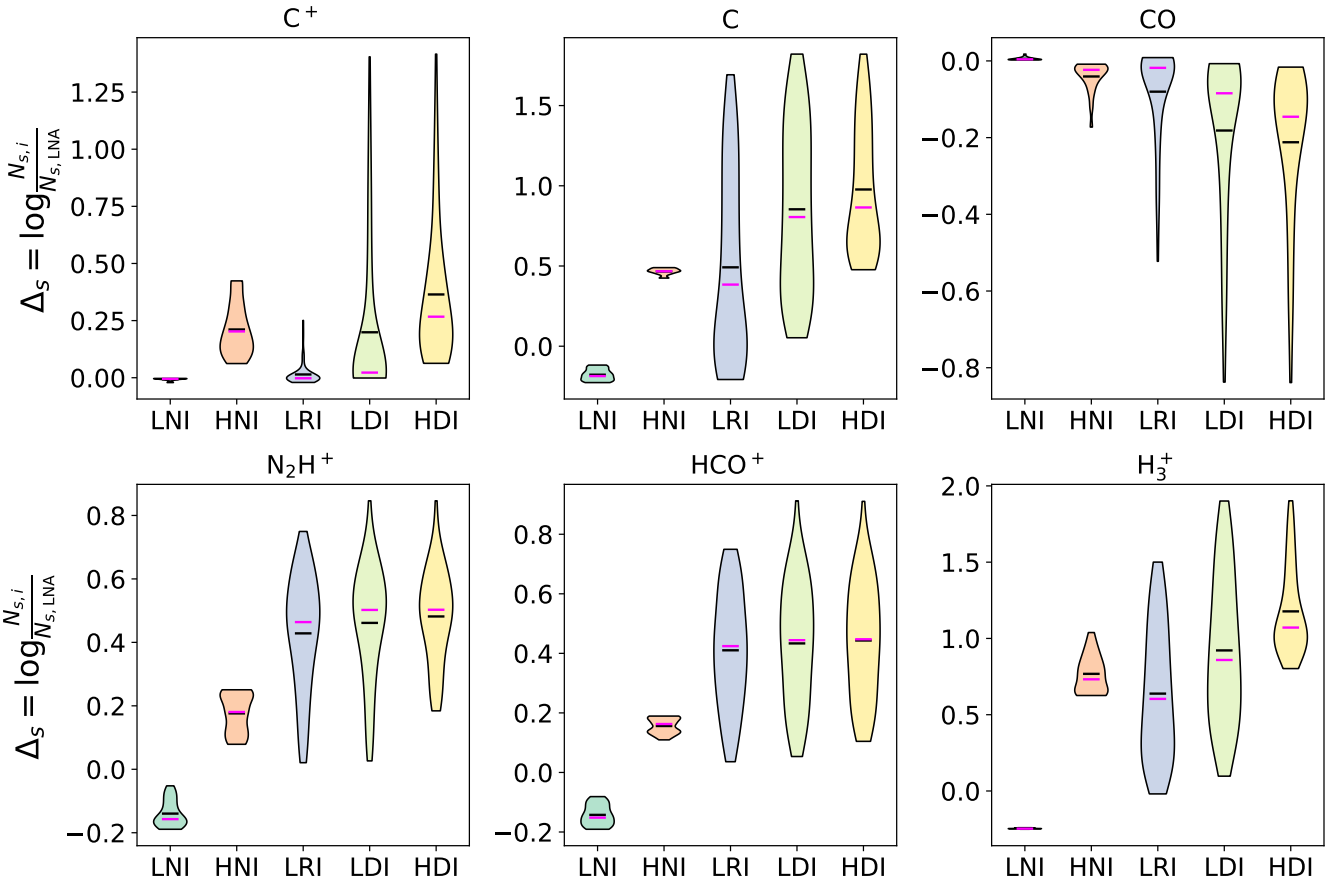


Figure 7. Logarithmic difference distribution, $\Delta_s = \log \frac{N_{s,i}}{N_{s,LNA}}$ comparing the difference in column density for molecular species, s, for five different cosmic ray models, $i \subset$ (LNI, HNI, LRI, LDI, HDI), compared to the LNA model. Distributions are generated using the model clouds across the (Σ_{cl} - N_*) parameter space. The black and magenta line indicate the mean and median, respectively.

4.2. *Comparison to Observed CRIRs*

Figure 11 shows the results from the different PDR models in Table 3 compared to four different observational surveys covering a range of $1 \leq A_V \leq 10^3$. The CRIR is one of the trickier astrochemical parameters to constrain from observations. Unfortunately, no universal method is applicable to all clouds conditions. Historically, there have been two main methods: absorption measurements of simple ions, such as H_3^+ or OH^+, in the infrared or molecular line observations using key molecules in neutral-ion pathways along with astrochemical modeling. H_3^+ is typically thought to be among the best tracers of the CRIR due to its simple chemistry. However, H_3^+ is only observed in infrared absorption, limiting its use to sight lines with bright background sources. Indriolo & McCall (2012) and Indriolo et al. (2015) used H_3^+, H_2O^+ and OH^+ absorption to trace the CRIR in diffuse gas with $A_V < 1$ and found the CRIR in low A_V gas varies between 10^{-16} -10^{-14} s^{-1}. The gas at low A_V is particularly sensitive to external influences, motivating the need to model the chemistry with external CR spectra derived from examining the local galactic environment. The grouping of points at low A_V with high CRIR ($\zeta \geq 10^{-14}$ s^{-1}) are clouds in sightlines towards the galactic center and thus in environments with extreme external particle irradiation. Caselli et al. (1998) used a combination of HCO^+, DCO^+ and CO together with analytic chemistry approximations to infer the CRIR in 24 dense cores. Their observations exhibit a nearly bi-model distribution: some are clustered at $\zeta \lessapprox 10^{-17}\,s^{-1}$, while the majority are at $\zeta \approx 10^{-16}\,s^{-1}$. They infer the ionization rates using the abundance ratios of [DCO^+/HCO^+] and [HCO^+]/[CO] under 0D spatial assumptions and a reduced analytic chemical network. Finally, we include the CRIRs from the van der Tak & van Dishoeck (2000) survey towards single high-mass protostars with the central protostar being massive enough to provide a bright background source for H_3^+ absorption. They find CRIRs scattered from 10^{-17} to 10^{-16} using an

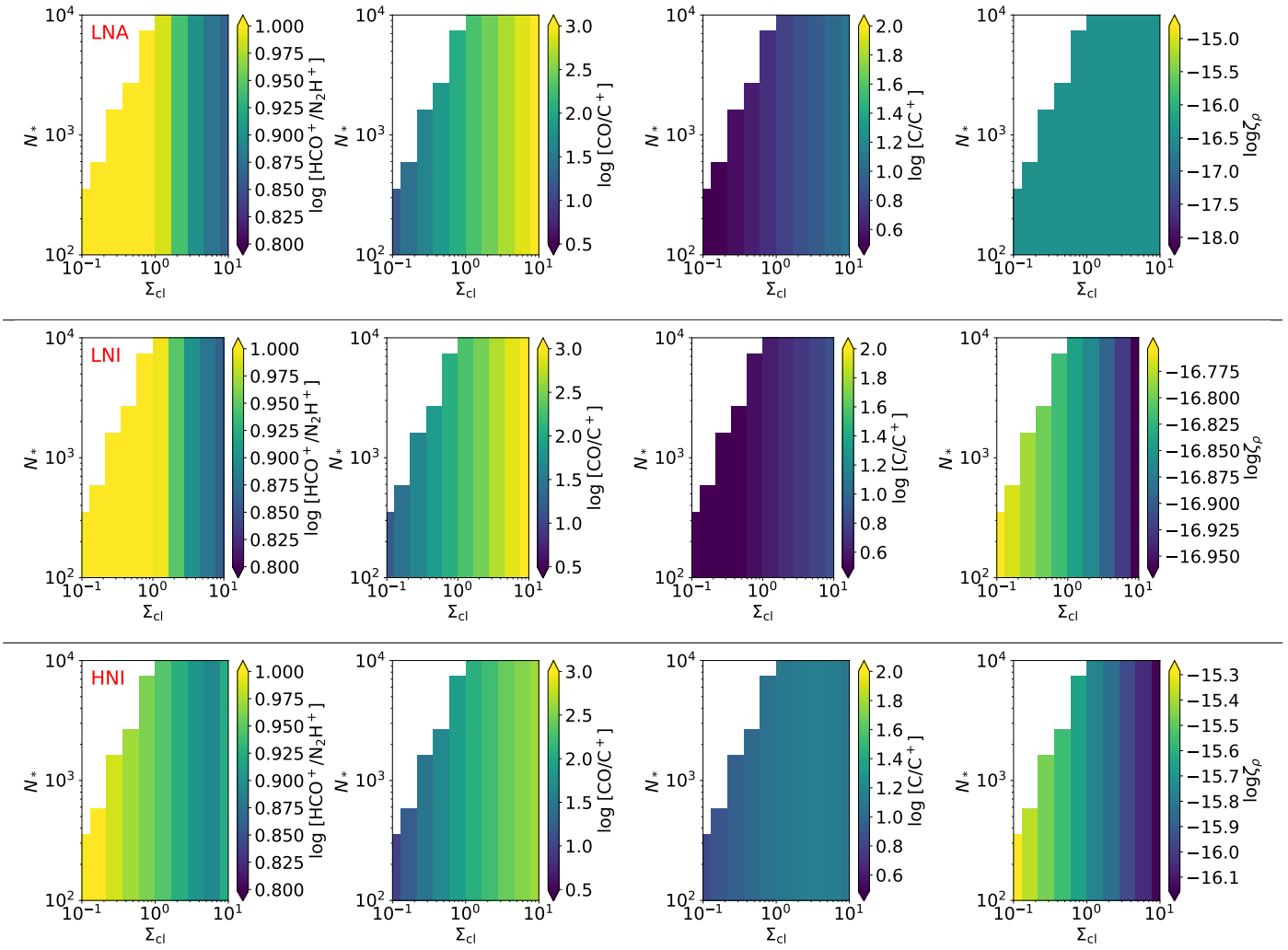


Figure 8. Abundance ratios versus Σ_{cl} and N_*. White contours and labels show the star formation efficiency $\varepsilon = M_*/M_{gas}$. Far left: $[HCO^+]/[N_2H^+]$. Middle left: $[CO/C^+]$. Middle right: $[C/C^+]$. Far right: Density-weighted average cosmic ray ionization rate, $< \zeta_\rho >$. The models are in descending order from top: LNA, LNI, HNI. We use the same scales for the individual ratios in Figures 8 and 9 to facilitate comparison between models.

assumed H_3^+ abundance and density distribution. They find the observed H_3^+ column density increases with cloud distance, which can be explained by contamination from low-density clouds along the line of sight.

Our model results show good agreement with the inferred CRIRs from Indriolo & McCall (2012), Indriolo et al. (2015) and Caselli et al. (1998). We find the LDI model is able to replicate the spread in the CRIR. There are two main controlling factors for the CRIR in the clouds: the number of embedded sources and the cloud environment. Embedded sources create a natural dispersion in ζ for different molecular cloud masses and star formation efficiencies. Without internal sources, there is no spread in our modelled CRIR as a function of column density. In order to represent the observations, the external CRIR must be increased instead for different regions. Local sources of CRs, such as nearby OB associations or supernova, contribute significantly to the CR flux at the cloud boundary. As the external CR flux is increased, the impact of attenuation also increases due to the rapid reduction in low energy CRs. Figure 11 shows that the impact of attenuation is different between the HNI and LNI models. For the LNI model, ζ changes by less than an order of magnitude across 4 orders of magnitude in A_V. Conversely, the HNI model CRIR decreases by 2 orders of magnitude due to an overall reduction in MeV-scale CRs. The HNI model over predicts the CRIRs measured in diffuse gas to CRIRs measured near high-mass protostars, excluding the galactic center sightlines. However, the $\mathcal{H}$ spectrum is the maximal CR spectrum from Voyager-1 observations (Stone et al. 2013; Ivlev et al. 2015). The LNI and

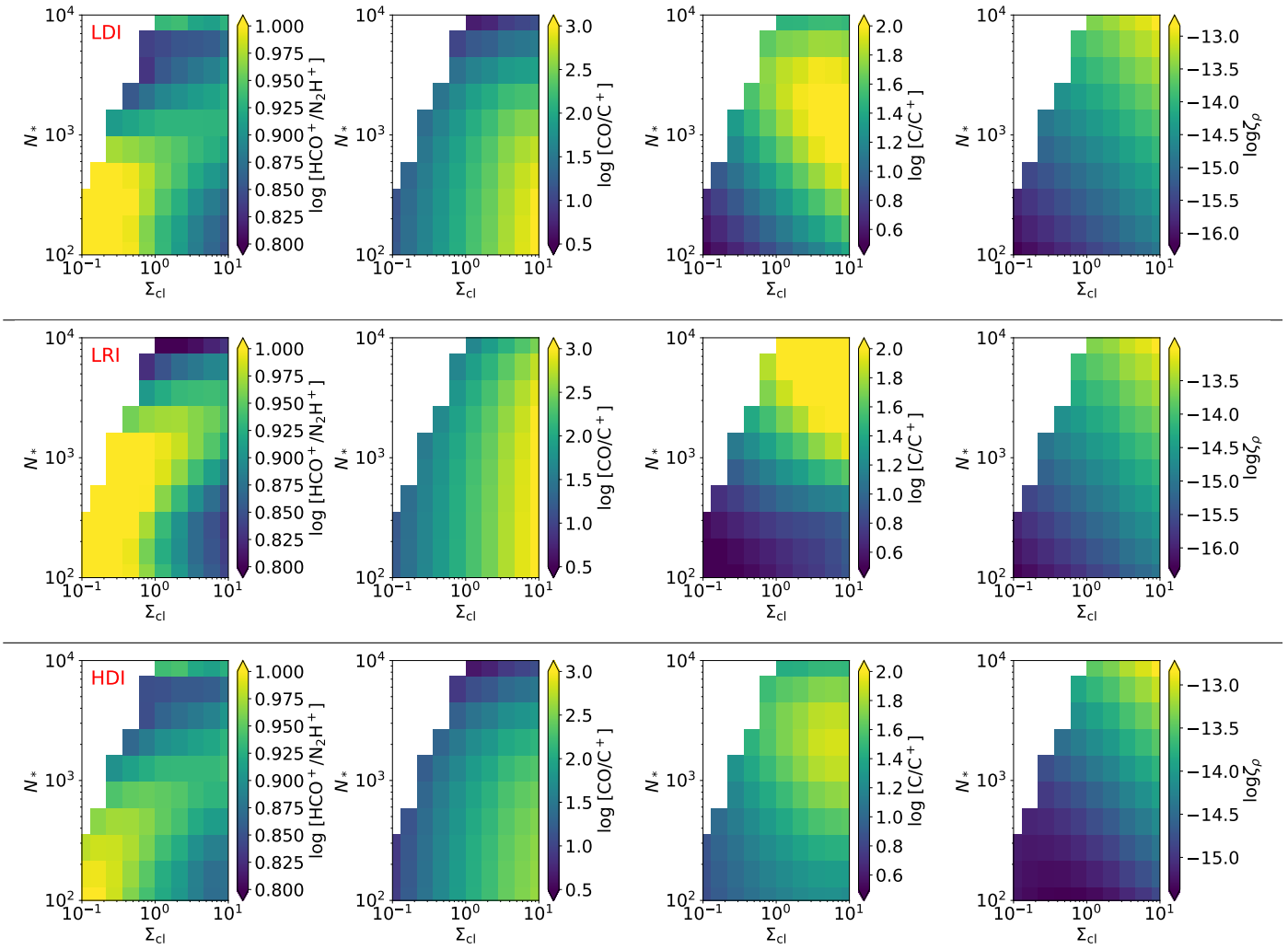


Figure 9. Abundance ratios versus Σ_{cl} and N_*. White contours and labels show the star formation efficiency $\varepsilon = M_*/M_{gas}$. Far left: $[HCO^+]/[N_2H^+]$. Middle left: $[CO/C^+]$. Middle right: $[C/C^+]$. Far right: Density-weighted average cosmic ray ionization rate, $< \zeta_\rho >$. Models in descending order from top: LDI, LRI, HDI

LNA models under-predict the observed CRIR for all but a few sight-lines. Thus, Figure 11 demonstrates that it is essential to consider the cloud environment and properly treat the CR physics and cloud density distributions. Models without attenuation only represent the CRIR within narrow ranges of A_V and not in the cloud interiors. Figure 11 also underscores that the low energy CR spectrum, which if often adopted in astrochemical modelling, is a poor fit to the majority of the observations.

4.3. *Challenges for Deriving the CRIR from Chemical Diagnostics*

There have been numerous attempts to find chemical diagnostics that are strong tracers of the CRIR (Caselli et al. 1998; Neufeld et al. 2010; Neufeld & Wolfire 2017; Indriolo et al. 2007; Indriolo & McCall 2012; Indriolo et al. 2015; Albertsson et al. 2018). Some of these, such as $[DCO^+]/[HCO^+]$, cannot be modelled with the current 3D-PDR version due to the lack of deuterium and isotopic chemistry. Most probes of the CRIR are based on the local abundance, which is difficult to directly ascertain from observations. The use of column density ratios typically assumes the line emission observed between species is co-spatial. Figures 8 and 9 examine effects of CR physics on the $[HCO^+/N_2H^+]$, $[CO/C^+]$ and $[C/C^+]$ column density ratio diagnostics. However, we find that none of these ratios are monotonically sensitive to the average CRIR, shown for the LDI model in Figure 5. The $[CO/C^+]$ column density ratio is anti-correlated with

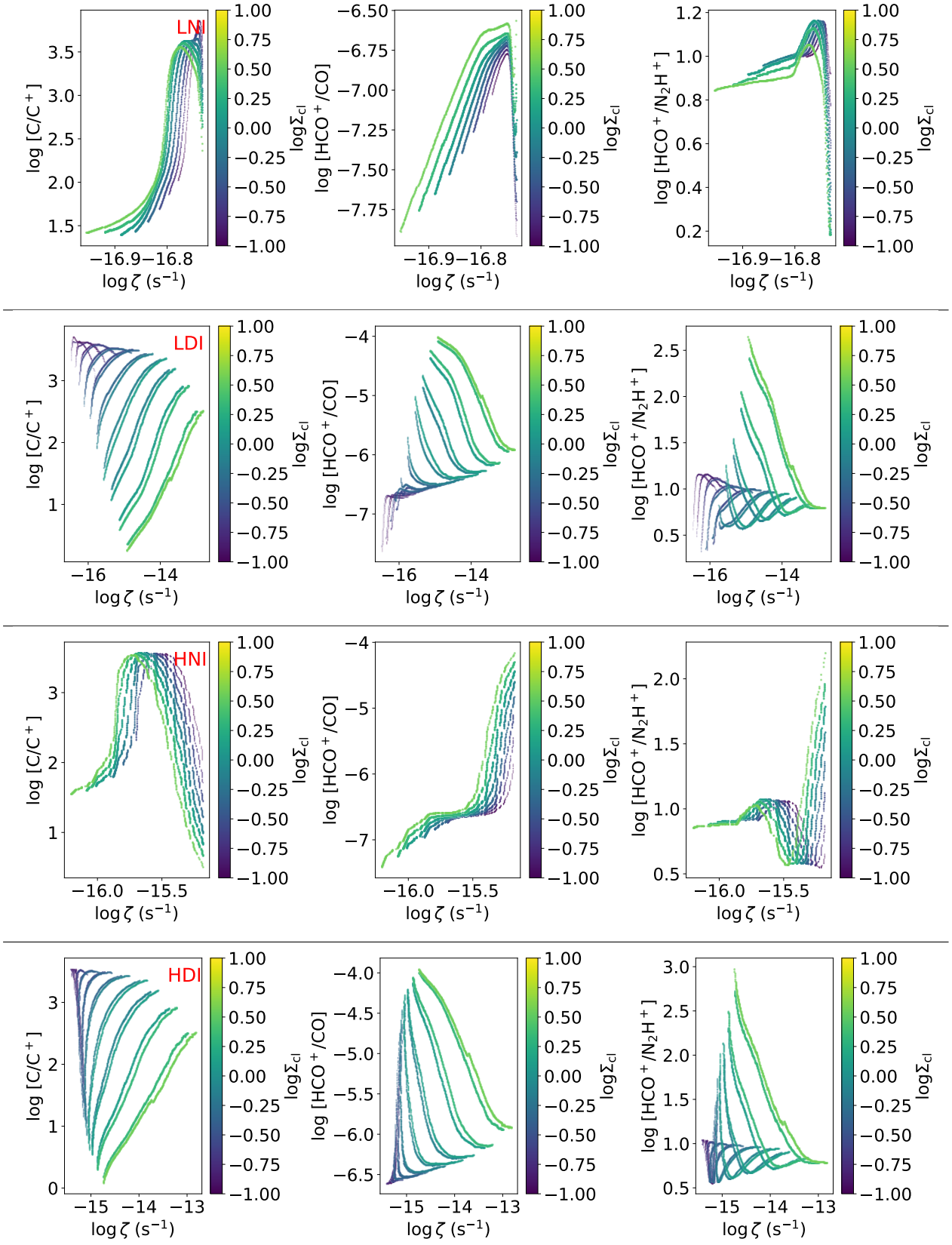


Figure 10. Cosmic ray ionization rate as a function of different abundance ratios. Left: C/C^+, middle: HCO^+/CO and right: HCO^+/N_2H^+. Models in descending order from top: LNI, LDI, HNI, HDI.

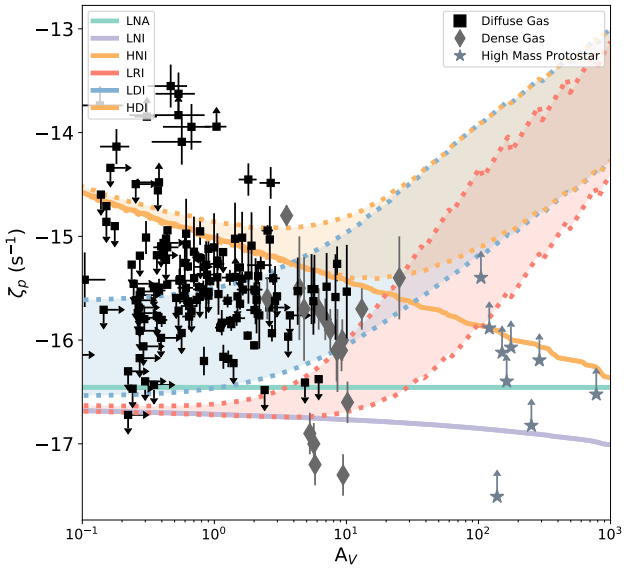


Figure 11. Cosmic ray ionization rate, ζ, versus A_V for the six different models in Table 3. The filled curves represent the 1σ spread from the models covering the ($\Sigma_{\rm cl}$ - N_*) parameter space. Squares represent diffuse gas measurements from Indriolo & McCall (2012) and Indriolo et al. (2015). Diamonds represent dense gas measurements from Caselli et al. (1998). Crosses represent observations towards high-mass protostars from de Boisanger et al. (1996); van der Tak & van Dishoeck (2000).

the density-averaged CRIR because the amount of CO declines while the amount of C^+ increases in large, massive clusters.

Local abundance ratios are used for fitting observations with astrochemical models which assume the ratio of the column densities is equal to the ratio of the abundances (Indriolo & McCall 2012). These are constrained through the use of 0-D spatial models, where a single density, temperature and extinction are evolved over time. However, this ignores the physical structure of clouds, which have non-uniform density, temperature, FUV and, as we show here, CRIR distributions (Clark et al. 2012; Offner et al. 2013; Gaches et al. 2015; Glover et al. 2015; Seifried et al. 2017). As Figure 10 shows, in models without internal sources, none of the abundance ratios are strong diagnostics. Furthermore, the range in the CRIR is small despite some large changes in each of the ratios. For models with internal sources, the CRs from embedded sources dominate the chemistry throughout the cloud. Here, we find the ratios of C/C^+ and HCO^+/CO are mostly monotonic with the CRIR. However, there is significant variation with $\Sigma_{\rm cl}$ and thus with the gas mass. The results signify that more careful physical and chemical modeling needs to be done to accurately constrain the CRIR in high-surface density, star-forming regions. The ratios are only a good diagnostic in regions where CRs dominate the thermo-chemistry.

Recently, Le Petit et al. (2016) used H_3^+ absorption to infer the CRIR and physical conditions in the CMZ. They used a similar relation to Equation 8:

$$N(H_3^+) = 0.96 \frac{\zeta L}{k_e} \frac{f}{2x_e}, \tag{11}$$

where k_e, f, and x_e have the same definition as in Equations 8 and 9 and L is the size of the cloud. They fit observed H_3^+ column densities with PDR models as a function of the gas density, n_H, and the size of the cloud, L. Most sightlines are well fit using their method by clouds with densities $10 \leq n_H \leq 100$ cm^{-3} corresponding to $5 \lesssim L \lesssim 100$ pc. Our models suggest that these length scales would incur CR screening effects which would change the CRIR. Similarly, for the high density clouds, the energy losses will deplete MeV CRs and reduce the CRIR. In these cases, there is a further degeneracy in the $n_H - L$ plane resulting in an average decrease in the CRIR. The reduction would systematically produce model fits with lower densities to correct for the lower CRIR.

Rimmer et al. (2012) used a similar hybrid approach, adopting a prescription for $\zeta(N)$ ad-hoc with the MEUDON PDR code Le Petit et al. (2006) to model the Horsehead Nebula. They found their high $\zeta(N_H)$ model improved agreement

over standard constant CRIR PDR prescriptions. However, their treatment of $\zeta(N)$ is static and fixed in time. The decoupling of CR attenuation and chemistry is only a good approximation if the abundance of neutral Hydrogen (H, H_2) does not change much in time, ensuring that the CR spectrum is constant in time. The new approach presented here will allow $\zeta(N)$ to be connected to the chemical time evolution.

4.4. *Impact of Cosmic Ray Feedback on Cloud Chemistry*

The *Herschel* Galactic Observations of Terahertz C+ (GOT C+) (Pineda et al. 2013) survey mapped [C II] 158 μm emission over the whole galactic disk, providing the best constraint on where [C II] emission originates. Pineda et al. (2013) found that nearly half of the [C II] emission originates from dense photon dominated regions with about another quarter of the emission from CO-dark H_2 gas. Clark et al. (2019) performed synthetic observations of young simulated molecular clouds and found the majority of their [C II] emission originates from atomic-Hydrogen dominated gas. This discrepancy was explained by the time evolution of molecular gas due to star formation and feedback. The results presented here provide an complementary explanation for the [C II]-bright molecular gas. When protoclusters become active, they accelerate CRs into the densest regions of molecular clouds. Figure 6 shows that high-mass protoclusters will lead to [C II]-bright H_2 dominated gas since CRs i) increase the gas temperature to values closer to the [C II] excitation temperature of 91.2 K, ii) increase the abundance of C^+ in dense gas due to the destruction of CO and iii) do not significantly alter the abundance of H_2.

In local star-forming regions, the lowest inversion transitions of ammonia, NH_3, have been widely used to map the dense gas cores within molecular clouds (i.e., Goodman et al. 1993; Jijina et al. 1999; Rosolowsky et al. 2008; Wienen et al. 2012). Ammonia remains optically thin, and while it does suffer from depletion, it's formation is enhanced in regions where CO freezes out (Caselli & Ceccarelli 2012) (although this effect is not included in our models). However, this also makes ammonia much more susceptible to local variations in the FUV radiation field, temperature and CRIR. Recently, the Green Bank Ammonia Survey (GAS) mapped all the Gould Belt clouds with $A_V > 7$ mag (Friesen et al. 2017). The DR1 data show the line-of-sight averaged abundance, $X(NH_3) = N(NH_3)/N(H_2)$, exhibits a spread through molecular clouds. The spread could be caused by the porosity of molecular clouds allowing more FUV radiation into regions of dense gas. However, our 1D models also exhibit a variation in this abundance measurement for the models with internal sources (LRI, LDI and HDI). Figure 6 shows that ammonia is depleted in clusters exhibiting more embedded star formation by a couple of orders of magnitude. The abundance within the dense gas goes from 10^{-8} in small clusters to 10^{-10} in the largest. Furthermore, the gas also heats up leading to stronger emission in higher transitions, such as NH_3(3,3). Redaelli et al. (2017) examined the NH_3 GAS map of the Barnard 59 clump in more detail. They found that the abundance appears to drop in gas around the central central 0/1 protostar. The dust temperature shows a clear increase around the same source with a slight increase in the ammonia excitation temperature.

4.5. *Impact of Cosmic Ray Feedback on Chemistry in Dense Cores*

Protostars are observed to be dimmer than classic collapse models predict, i.e., the "Protostellar Luminosity Problem" (Dunham et al. 2014). One possible solution is that accretion is strongly episodic (Kenyon et al. 1990; Vorobyov 2009; Offner & McKee 2011). Although our models assume steady-state accretion, we can infer the impact of large bursts of accretion on cloud chemistry. An accretion burst leads to a stronger accretion shock, which in turn produces higher energy CRs and a higher CRIR. The CRIR increase in the dense gas then raises the temperature. The higher temperatures, whether caused by radiative or CR heating, lead to several different chemical effects. First, molecules frozen onto dust grains will evaporate, both by thermal desorption (Öberg 2016) and CR-induced desorption Hasegawa & Herbst (1993), into the gas phase. Second, the increase of the CRIR will increase the ionization fraction leading to a chain of ion-neutral reactions following H_3^+. Finally, the elevated radiative and CR flux may be strong enough to destroy some molecules. Jørgensen et al. (2015) and Frimann et al. (2016) showed that episodic accretion can cause the sublimation of CO-ice and explain the excess $C^{18}O$ emission observed near protostars. Intuitively, a burst a CRs will lead to a reaction chain: H_3^+ is created, thereby leading to the destruction of CO to form HCO^+. However, the increase in CRs will provide a large population of free electrons which recombine with HCO^+ to form CO. HCO^+ also interacts with water and other dipole neutrals (in the case of water, the reaction leads to the formation of CO and protonated water). HCO^+ is observed to be depleted near protostars that have undergone episodic accretion (Jørgensen et al. 2013). Ices sublimated by an accretion burst will cause a more active gas-phase chemistry and lead to an increase in carbon-chain molecules in molecular clouds as well as increase gas-phase CO in the dense gas where

it would otherwise freeze-out. Overall, the addition of CRs magnifies the effect of an accretion burst. Temperatures increase beyond that expected from radiative heating alone. This suggests that a smaller change in accretion rate may be needed to produce the observed chemical changes.

4.6. *Implications for Comparing Data and Models*

Synthetic observations of hydro-dynamic simulations are a vital tool for comparing theoretical predictions to observations. The synthetic observations may treat the chemistry in different ways: from assuming a constant abundance of some molecule to post-processing simulations with an astrochemical code or using the reduced-network chemistry from the hydrodynamic simulation (see review by Haworth et al. 2018). These synthetic observations are used to gauge how well the simulations correspond to the observed universe. As such, it is paramount to ensure that all astrochemical parameters are as accurate as possible. Radiation-MHD simulations can provide the density and temperature at every point (e.g., Offner et al. 2009). Simulations also now often include FUV radiation and optical depth calculations using packages such as FERVENT (Baczynski et al. 2015), TREERAY (Wünsch et al., in preparation, used in Haid et al. (2019)) and HARM^2 (Rosen et al. 2017). These methods can provide the FUV radiation and/or optical depth into the cloud. Our results, here, show that the H_2 optical depth into the cloud should be considered when calculating the appropriate CRIR for post-processing. Typically, the CRIR is held constant throughout the entire simulation domain, which will lead to systematic differences in the simulation line emission.

5. CONCLUSIONS

We implement cosmic-ray attenuation in the public astrochemistry code 3D-PDR. The implementation uses the H_2 column density from the chemistry to attenuate the CR spectra. We couple the code to the protostellar CR models from Gaches & Offner (2018b), which solve for the total attenuated protocluster CR spectrum as a function of the cloud surface density, $\Sigma_{\rm cl}$, and number of constituent protostars, N_*. We present one-dimensional astrochemical models for molecular clouds with a wide range of $\Sigma_{\rm cl}$ and N_*. We compare the abundance distributions for a low external CR spectrum, representing an extrapolation of the Voyager-1 data, and a high external CR spectrum, representing a maximal correction for solar influences. Our model results show that CRs originating from the accretion shocks of protostars affect the chemistry of the surrounding molecular cloud. We conclude the following:

- Models with no sources or attenuation cannot explain observed CRIRs. Models with no internal sources but a higher ($\mathcal{H}$) external spectrum (HNI) match the observed CRIRs, although it may under-predict the CRIRs inferred for high-mass protostars. We find that a model using the commonly adopted spectrum with internal sources (LDI) matches both the low and mid A_V observations of ζ and the observed spread.

- CRs accelerated by protostellar accretion shocks significantly alter the Carbon chemistry in star-forming clouds. The amount of neutral and ionized Carbon increases in the dense gas as the number of protostars increases. Models with embedded sources (LDI, LRI, HDI) increase the amount of C, HCO^+ and NH_3 at lower A_V and decrease the abundance of CO and NH_3 at higher A_V. Overall, models including internal sources (LDI, LRI and HDI) exhibit a higher abundance of HCO^+ and H_3^+ with $\Sigma_{\rm cl}$ and N_*.

- Approximations that use H_3^+ and C-based tracers to estimate the CRIR systematically under-predict the CRIR unless CRs are the dominant source of ionization. The Reduced Analytic Approximation, which uses the abundances of H_3^+, CO and O,always produces more accurate values of the CRIR, highlighting the importance of obtaining accurate Oxygen and Carbon Monoxide abundances within molecular clouds.

- Ions are systematically under produced using the canonical CRIR while CO is over produced. Internal sources created a dispersion in the distribution of column densities by driving more active ion-neutral chemistry deep within molecular clouds.

- Models using the low external CR spectrum ($\mathcal{L}$) and/or no internal sources of CRs under estimate the H_3^+ column density by a order of magnitude or more.

- Internally-accelerated CRs will naturally lead to molecular gas which become CO-deficient but [C II]-bright, particularly for high surface density molecular clouds hosting large clusters.

- Including CR attenuation in PDR models will help break the denegeracy in astrochemical modeling between the density, CRIR and FUV radiation.

As protoclusters grow in constituent nubmers, the impact on the chemistry is amplified, greatly so if CRs diffuse out of molecular clouds rather than stream. Comparison to observed CRIRs suggest the external CR spectrum, attenuation and internal sources are important for modelling the chemistry of molecular clouds. However, the current uncertainties are large due to lack of observational data that can simultaneously constrain the density, FUV radiation and CRIR on molecular cloud scales. Observations to constrain the CRIR within dense gas necessitate multi-line data, to independently determine the temperature as in e.g., Ceccarelli et al. (2014), and multi-species data, to act as astrochemical diagnostics as in e.g., Caselli et al. (1998). The 3D-PDR CR attenuation FORTRAN module can be included in any FORTRAN astrochemistry code.

Facility: Massachusetts Green High Performance Computing Center

Software:

- 3D-PDR (Bisbas et al. 2012)
- MATPLOTLIB (Hunter 2007)
- NUMPY (van der Walt et al. 2011)
- SCIPY (Jones et al. 2001–)
- JUPYTERLAB

SSRO and BALG acknowledge support from the National Science Foundation (NSF) grant AST-1510021. SSRO was also supported by NSF CAREER grant AST-1650486. TGB acknowledges funding by the German Science Foundation (DFG) via the Collaborative Research Center SFB 956 "Conditions and impact of star formation". The authors thank helpful discussions with Neal Evans and Nick Indriolo and the anonymous referee for their useful comments. The calculations performed for this work were done on the Massachusetts Green High Performance Computing Center (MGHPCC) in Holyoke, Massachusetts supported by the University of Massachusetts, Boston University, Harvard University, MIT, Northeastern University and the Commonwealth of Massachusetts.

REFERENCES

Albertsson, T., Kauffmann, J., & Menten, K. M. 2018, ApJ, 868, 40

Baczynski, C., Glover, S. C. O., & Klessen, R. S. 2015, MNRAS, 454, 380

Bayet, E., Williams, D. A., Hartquist, T. W., & Viti, S. 2011, MNRAS, 414, 1583

Bell, T. A., Roueff, E., Viti, S., & Williams, D. A. 2006, MNRAS, 371, 1865

Bertoldi, F., & McKee, C. F. 1992, ApJ, 395, 140

Bisbas, T. G., Bell, T. A., Viti, S., Yates, J., & Barlow, M. J. 2012, MNRAS, 427, 2100

Bisbas, T. G., Papadopoulos, P. P., & Viti, S. 2015, ApJ, 803, 37

Bisbas, T. G., Schruba, A., & van Dishoeck, E. F. 2019, MNRAS, 485, 3097

Bisbas, T. G., van Dishoeck, E. F., Papadopoulos, P. P., et al. 2017, ApJ, 839, 90

Bisbas, T. G., Tan, J. C., Csengeri, T., et al. 2018, MNRAS, 478, L54

Caselli, P., & Ceccarelli, C. 2012, A&ARv, 20, 56

Caselli, P., Walmsley, C. M., Terzieva, R., & Herbst, E. 1998, ApJ, 499, 234

Ceccarelli, C., Dominik, C., López-Sepulcre, A., et al. 2014, ApJ, 790, L1

Clark, P. C., Glover, S. C. O., Klessen, R. S., & Bonnell, I. A. 2012, MNRAS, 424, 2599

Clark, P. C., Glover, S. C. O., Ragan, S. E., & Duarte-Cabral, A. 2019, MNRAS, 1076

Clark, P. C., Glover, S. C. O., Ragan, S. E., Shetty, R., & Klessen, R. S. 2013, ApJL, 768, L34

Cleeves, L. I., Bergin, E. A., & Adams, F. C. 2014, ApJ, 794, 123

Dalgarno, A. 2006, PNAS, 103, 12269

Dalgarno, A., & Griffing, G. W. 1958, RSPSA, 248, 415

de Boisanger, C., Helmich, F. P., & van Dishoeck, E. F. 1996, A&A, 310, 315

Draine, B. T. 2011, Physics of the Interstellar and Intergalactic Medium (Princeton University Press)

Drury, L. O. 1983, RPPh, 46, 973

Dunham, M. M., Stutz, A. M., Allen, L. E., et al. 2014, in Protostars and Planets VI, ed. H. Beuther, R. S. Klessen, C. P. Dullemond, & T. Henning, 195
Evoli, C., Gaggero, D., Vittino, A., et al. 2017, JCAP, 2017, 015
Favre, C., López-Sepulcre, A., Ceccarelli, C., et al. 2017, A&A, 608, A82
Favre, C., Ceccarelli, C., López-Sepulcre, A., et al. 2018, ApJ, 859, 136
Federman, S. R., Rawlings, J. M. C., Taylor, S. D., & Williams, D. A. 1996, MNRAS, 279, L41
Fontani, F., Ceccarelli, C., Favre, C., et al. 2017, A&A, 605, A57
Friesen, R. K., Pineda, J. E., co-PIs, et al. 2017, ApJ, 843, 63
Frimann, S., Jørgensen, J. K., Padoan, P., & Haugbølle, T. 2016, A&A, 587, A60
Gaches, B. A. L., & Offner, S. S. R. 2018a, ApJ, 854, 156
—. 2018b, ApJ, 861, 87
Gaches, B. A. L., Offner, S. S. R., Rosolowsky, E. W., & Bisbas, T. G. 2015, ApJ, 799, 235
Girichidis, P., Naab, T., Walch, S., et al. 2016, ApJ, 816, L19
Glover, S. C. O., Clark, P. C., Micic, M., & Molina, F. 2015, MNRAS, 448, 1607
Goodman, A. A., Benson, P. J., Fuller, G. A., & Myers, P. C. 1993, ApJ, 406, 528
Grenier, I. A., Black, J. H., & Strong, A. W. 2015, ARA&A, 53, 199
Haid, S., Walch, S., Seifried, D., et al. 2019, MNRAS, 482, 4062
Hartmann, L., Herczeg, G., & Calvet, N. 2016, ARA&A, 54, 135
Hasegawa, T. I., & Herbst, E. 1993, MNRAS, 261, 83
Haworth, T. J., Glover, S. C. O., Koepferl, C. M., Bisbas, T. G., & Dale, J. E. 2018, NewAR, 82, 1
Heyer, M., & Dame, T. M. 2015, ARA&A, 53, 583
Hollenbach, D., Kaufman, M. J., Neufeld, D., Wolfire, M., & Goicoechea, J. R. 2012, ApJ, 754, 105
Hunter, J. D. 2007, CSE, 9, 90
Indriolo, N., Geballe, T. R., Oka, T., & McCall, B. J. 2007, ApJ, 671, 1736
Indriolo, N., & McCall, B. J. 2012, ApJ, 745, 91
Indriolo, N., Neufeld, D. A., Gerin, M., et al. 2015, ApJ, 800, 40
Ivlev, A. V., Padovani, M., Galli, D., & Caselli, P. 2015, ApJ, 812, 135
Jijina, J., Myers, P. C., & Adams, F. C. 1999, ApJS, 125, 161
Jones, E., Oliphant, T., Peterson, P., et al. 2001–, SciPy: Open source scientific tools for Python, , , [Online;]
Jørgensen, J. K. 2004, A&A, 424, 589
Jørgensen, J. K., Visser, R., Williams, J. P., & Bergin, E. A. 2015, A&A, 579, A23
Jørgensen, J. K., Visser, R., Sakai, N., et al. 2013, ApJ, 779, L22
Karpas, Z., Anicich, V., & Huntress, W. T. 1979, JChPh, 70, 2877
Kenyon, S. J., Hartmann, L. W., Strom, K. M., & Strom, S. E. 1990, AJ, 99, 869
Kirk, J. G. 1994, in Saas-Fee Advanced Course 24: Plasma Astrophysics, 225
Klippenstein, S. J., Georgievskii, Y., & McCall, B. J. 2010, JPCA, 114, 278
Krause, J., Morlino, G., & Gabici, S. 2015, in 34th International Cosmic Ray Conference (ICRC2015), Vol. 34, 518
Le Petit, F., Nehmé, C., Le Bourlot, J., & Roueff, E. 2006, ApJS, 164, 506
Le Petit, F., Ruaud, M., Bron, E., et al. 2016, A&A, 585, A105
McCall, B. J., Huneycutt, A. J., Saykally, R. J., et al. 2004, PhRvA, 70, 052716
McElroy, D., Walsh, C., Markwick, A. J., et al. 2013, A&A, 550, A36
McKee, C. F. 1989, ApJ, 345, 782
McKee, C. F., & Ostriker, E. C. 2007, ARA&A, 45, 565
McKee, C. F., & Tan, J. C. 2003, ApJ, 585, 850
Meijerink, R., Spaans, M., Loenen, A. F., & van der Werf, P. P. 2011, A&A, 525, A119
Melrose, D. B. 2009, in Encyclopedia of Complexity and Systems Science, ed. R. A. Meyers (Springer), 21–42
Mitchell, J. B. A. 1990, PhR, 186, 215
Moskalenko, I. V., & Strong, A. W. 1998, ApJ, 493, 694
Moskalenko, I. V., Strong, A. W., & Mashnik, S. G. 2005, in American Institute of Physics Conference Series, Vol. 769, International Conference on Nuclear Data for Science and Technology, ed. R. C. Haight, M. B. Chadwick, T. Kawano, & P. Talou, 1612–1617
Neufeld, D. A., & Wolfire, M. G. 2017, ApJ, 845, 163
Neufeld, D. A., Goicoechea, J. R., Sonnentrucker, P., et al. 2010, A&A, 521, L10
Öberg, K. I. 2016, ChRv, 116, 9631, pMID: 27099922
Offner, S. S. R., Bisbas, T. G., Bell, T. A., & Viti, S. 2014, MNRAS, 440, L81
Offner, S. S. R., Bisbas, T. G., Viti, S., & Bell, T. A. 2013, ApJ, 770, 49
Offner, S. S. R., Klein, R. I., McKee, C. F., & Krumholz, M. R. 2009, ApJ, 703, 131

Offner, S. S. R., & McKee, C. F. 2011, ApJ, 736, 53
Padovani, M., Galli, D., & Glassgold, A. E. 2009, A&A, 501, 619
Padovani, M., Ivlev, A. V., Galli, D., & Caselli, P. 2018, A&A, 614, A111
Padovani, M., Marcowith, A., Hennebelle, P., & Ferrière, K. 2016, A&A, 590, A8
Pety, J., Guzmán, V. V., Orkisz, J. H., et al. 2017, A&A, 599, A98
Pineda, J. L., Langer, W. D., Velusamy, T., & Goldsmith, P. F. 2013, A&A, 554, A103
Pound, M. W., & Yusef-Zadeh, F. 2018, MNRAS, 473, 2899
Redaelli, E., Alves, F. O., Caselli, P., et al. 2017, ApJ, 850, 202
Rimmer, P. B., Herbst, E., Morata, O., & Roueff, E. 2012, A&A, 537, A7
Rodgers-Lee, D., Taylor, A. M., Ray, T. P., & Downes, T. P. 2017, MNRAS, 472, 26
Rosen, A. L., Krumholz, M. R., Oishi, J. S., Lee, A. T., & Klein, R. I. 2017, JCoPh, 330, 924
Rosolowsky, E. W., Pineda, J. E., Foster, J. B., et al. 2008, ApJS, 175, 509
Schlickeiser, R. 2002, Cosmic Ray Astrophysics (Springer)
Schlickeiser, R., Caglar, M., & Lazarian, A. 2016, ApJ, 824, 89
Seifried, D., Walch, S., Girichidis, P., et al. 2017, MNRAS, 472, 4797
Sembach, K. R., Howk, J. C., Ryans, R. S. I., & Keenan, F. P. 2000, ApJ, 528, 310
Shu, F. H. 1977, ApJ, 214, 488
Stone, E. C., Cummings, A. C., McDonald, F. B., et al. 2013, Sci, 341, 150
Storm, S., Mundy, L. G., Lee, K. I., et al. 2016, ApJ, 830, 127
Strong, A. W., & Moskalenko, I. V. 2001, AdSpR, 27, 717
Strong, A. W., Moskalenko, I. V., & Ptuskin, V. S. 2007, ARNPS, 57, 285
Takayanagi, K. 1973, PASJ, 25, 327
Theard, L. P., & Huntress, W. T. 1974, JChPh, 60, 2840
van der Tak, F. F. S., & van Dishoeck, E. F. 2000, A&A, 358, L79
van der Walt, S., Colbert, S. C., & Varoquaux, G. 2011, CSE, 13, 22
van Dishoeck, E. F. 2014, FaDi, 168, 9
Visser, R., van Dishoeck, E. F., & Black, J. H. 2009, A&A, 503, 323
Vorobyov, E. I. 2009, ApJ, 704, 715
Wakelam, V., Cuppen, H. M., & Herbst, E. 2013, arXiv, arXiv:1309.7792
Watson, W. D. 1976, RvMP, 48, 513
Wienen, M., Wyrowski, F., Schuller, F., et al. 2012, A&A, 544, A146